

Asymptotic analysis and design of linear elastic shell lattice metamaterials

DI ZHANG, University of Science and Technology of China, China

LIGANG LIU*, University of Science and Technology of China, China

We present an asymptotic analysis of shell lattice metamaterials based on Ciarlet’s shell theory, introducing a new metric—*asymptotic directional stiffness* (ADS)—to quantify how the geometry of the middle surface governs the effective stiffness. We prove a convergence theorem that rigorously characterizes ADS and establishes its upper bound, along with necessary and sufficient condition for achieving it. As a key result, our theory provides the first rigorous explanation for the high bulk modulus observed in Triply Periodic Minimal Surfaces (TPMS)-based shell lattices. To optimize ADS on general periodic surfaces, we propose a triangular-mesh-based discretization and shape optimization framework. Numerical experiments validate the theoretical findings and demonstrate the effectiveness of the optimization under various design objectives. Our implementation is available at <https://github.com/lavenklau/minisurf>.

CCS Concepts: • **Computing methodologies** → **Computer graphics**; **Model development and analysis**; • **Mathematics of computing** → **Partial differential equations**.

Additional Key Words and Phrases: TPMS, Shell, Lattice metamaterial, Asymptotic analysis

ACM Reference Format:

Di Zhang and Ligang Liu. 2025. Asymptotic analysis and design of linear elastic shell lattice metamaterials. *ACM Trans. Graph.* 44, 4 (August 2025), 18 pages. <https://doi.org/10.1145/3730888>

1 Introduction

The application of Triply Periodic Minimal Surfaces (TPMS) in metamaterial design has achieved great success in recent decades [Feng et al. 2022]. Numerous simulation and experimental studies have demonstrated their superior stiffness and strength properties [Chen et al. 2019; Deng and Cheng 2021; Wang et al. 2022c]. However, these findings are primarily empirical, derived from studies on a limited number of TPMS configurations. The fundamental mechanisms underlying their exceptional performance are still not fully understood, and it remains unclear whether these advantages generalize to all TPMS configurations.

Since TPMS typically serve as the middle surface of the shell lattice metamaterials [Feng et al. 2022; Ma et al. 2021, 2022; Wang et al. 2022c], understanding how middle surface geometry influences effective stiffness provides a natural starting point for theoretical

*Corresponding author.

Authors’ Contact Information: Di Zhang, zhd9702@mail.ustc.edu.cn, University of Science and Technology of China, Hefei, China; Ligang Liu, University of Science and Technology of China, Hefei, China, lgliu@ustc.edu.cn.

Permission to make digital or hard copies of all or part of this work for personal or classroom use is granted without fee provided that copies are not made or distributed for profit or commercial advantage and that copies bear this notice and the full citation on the first page. Copyrights for components of this work owned by others than the author(s) must be honored. Abstracting with credit is permitted. To copy otherwise, or republish, to post on servers or to redistribute to lists, requires prior specific permission and/or a fee. Request permissions from permissions@acm.org.

© 2025 Copyright held by the owner/author(s). Publication rights licensed to ACM.
ACM 1557-7368/2025/8-ART
<https://doi.org/10.1145/3730888>

investigation. To this end, we introduce a novel metric called the *asymptotic directional stiffness* (ADS), defined as the limiting ratio of stiffness to volume fraction as shell thickness approaches zero. This metric captures the intrinsic relationship between surface geometry and effective stiffness, independent of thickness effects. By extending key results from Ciarlet’s shell theory [Ciarlet and Lods 1996a], we derive a convergence theorem that rigorously formulates ADS. Based on this theorem, we establish an upper bound for ADS, as well as the necessary and sufficient condition to achieve this bound. This condition implies the optimal asymptotic bulk modulus (i.e., the ADS under hydrostatic strain) of TPMS as a special case, thus explains previous experimental discoveries [Deng and Cheng 2021].

For practical applications, we develop a numerical approach to enhance the ADS of middle surfaces through shape optimization. Our method features a specialized triangular mesh discretization scheme that handles diverse surface topologies and shapes while supporting various optimization objectives. Unlike traditional shell structure optimization methods [Ma et al. 2022; Ramm et al. 1993; Shimoda and Liu 2014], our formulation decouples the geometry of the middle surface from thickness, enabling the direct search for optimal surface shapes without prescribing thickness-related parameters. Our contributions are summarized as follows

- We introduce the asymptotic directional stiffness (ADS) for shell lattice metamaterial and establish the convergence theorem that formalizes it.
- We establish the upper bound of ADS and the necessary and sufficient condition to achieve the bound. This result is used to justify the optimal bulk modulus of TPMS.
- A novel discretization scheme on triangular mesh that allows us to evaluate and optimize ADS.

2 Related work

Linear elastic mechanical metamaterial. The foundation for the design of linear elastic metamaterials is the homogenization theory, which determines the effective properties of the metamaterial by solving a *cell problem* on the representative volume element (RVE). Notable monographs on this topic include [Allaire 2002; Milton 2002]. In the graphics community, early works aim to construct microstructure families with prescribed elastic properties by interpolation from samplings [Schumacher et al. 2015] or through optimization on a set of parameterized geometry [Panetta et al. 2017, 2015]. The constructed microstructure family achieves a wide range of elastic properties. Besides the regular structures, other approaches explore the irregular foam structures, either based on Voronoi diagram [Martínez et al. 2016, 2018] or generated from stochastic process [Martínez et al. 2017]. Following a similar spirit, [Martínez et al. 2019] employs the generalized Voronoi diagrams induced by novel star-shaped metrics to improve the aesthetic. [Schumacher et al. 2018] explored the structured sheet materials based

on isohedral tilings that covers a wide range of material properties. Given that these designed structures typically cannot conform to an arbitrary boundary of the model, [Tozoni et al. 2020] introduced the rhombic microstructure with far greater flexibility in shape approximation. To enlarge the design space, [Makatura et al. 2023] developed a procedural framework to model microstructures by combining various constitutive elements, such as straight/curved beams, thin shells, and solid bulk materials. A similar approach is seen in [Liu et al. 2024], which integrates truss, plate, and shell structures into a multilayer design strategy.

Application of TPMS. The application studies based on TPMS have been exceptionally active in the last decade, we kindly refer the reader to the survey article [Feng et al. 2022] for a comprehensive overview. It has become a consensus in the community that TPMS exhibit superior stiffness. However, such understanding remains largely empirical, originating from numerical simulations and physical experiments on limited types of TPMS [Al-Ketan et al. 2020; Chen et al. 2019; Feng et al. 2021; Kaur and Singh 2021; Qureshi et al. 2021; Torquato and Donev 2004; Wang et al. 2022c]. Due to the lack of theoretical analysis, the underlying reason behind these discoveries is still unclear, and one cannot guarantee that all TPMS, including those yet to be undiscovered, have the same advantageous properties. In the graphics community, TPMS have been used to design inner supporting structures in 3D models to enhance stiffness [Hu et al. 2022; Xu et al. 2024; Yan et al. 2020] and improve heat dissipation [Wang et al. 2022a]. These works either focus on designing structures at a macroscopic scale rather than developing metamaterials or concentrate on limited types of TPMS, resulting in a lack of general conclusions.

Asymptotic analysis. Our analysis of shells is inspired by the serial works [Ciarlet and Lods 1996a,b; Ciarlet et al. 1996], in which limit equations for three types of shells—membrane shells, flexural shells, and generalized membrane shells—are derived. However, from a rigorous standpoint, directly applying these equations to our problem is not feasible for several reasons. First, the boundary conditions differ from theirs. Second, these shell equations rely on specific geometry assumptions on the middle surface that may not be satisfied by an arbitrary periodic surface. Third, a general periodic middle surface, due to its non-trivial topology, cannot be covered by a single coordinate chart, which is a common assumption behind these theories. Thus, technical adaptations of their theoretic results are necessary before the application. Another crucial distinction in our problem is that we are studying the convergence of a scalar quantity instead of the vector field. This allows us to establish a very general and concise conclusion without the need to classify different types of shells, as we will show in Section 4.

Simulation and optimization of shell structures. The existing works can be broadly classified into two categories: parametric and non-parametric methods. Parametric approaches typically use NURBS [Cai et al. 2023; Hirschler et al. 2019; Jiang et al. 2023; Kang and Youn 2016; Kiendl et al. 2014] or Bézier [Bletzinger and Ramm 1993; Ramm et al. 1993] patches to represent the middle surface of shells. The optimized shapes are restricted by the parameterization. In contrast, non-parametric approaches offer a free-form design, where

the middle surface is represented as a discrete mesh [Shimoda and Liu 2014], a subdivision surface [Bandara and Cirak 2018], or the level set of a function [Kobayashi et al. 2024]. Their derivation of the shape sensitivity is typically more involved than the parametric approaches. For simulation, the Kirchhoff-Love shell model is commonly used for analysis on the higher-order representations, such as NURBS [Hughes et al. 2005] or subdivision surfaces [Bandara and Cirak 2018]. When the geometry is approximated by a discrete mesh, facet-based shell elements are widely adopted in engineering for FEM simulations [Reddy 2006]. Each element is considered as a small plate whose deformation follows either the Kirchhoff [Kirchhoff 1850; Love 1888] or Mindlin hypothesis [Mindlin 1951]. In the graphics community, various discrete shell models [Grinspun et al. 2003; Narain et al. 2013] and solid shell elements [Montes Maestre et al. 2023] have been developed to facilitate the physical simulation of cloths, thin sheets, and geometry optimization tasks. The primary objective of traditional form-finding of shell is to minimize bending effects under prescribed loads [Bletzinger et al. 2010; Bletzinger and Ramm 1993; Bletzinger et al. 2005; Marmo and Vaiana 2021], or to construct self-supported shells in a purely membrane stress state [Ma et al. 2019; Miki and Mitchell 2022, 2024; Xing et al. 2024]. Other methods aim to minimize compliance [Jiang et al. 2023] or stress [Zhang et al. 2020].

Most of the aforementioned works focus on the design of macroscopic shell structures. To obtain a comprehensive overview of the mechanical properties of shell lattice metamaterials, [Bonatti and Mohr 2019] carried out extensive finite element simulations on various TPMS-based cubic shell lattices. [Chen et al. 2020] designed several stretching-dominated shell lattices that can absorb very large energies while retaining a low density. [Ma et al. 2021, 2022] leveraged the cubic symmetry of several TPMS configurations, employing NURBS to represent the symmetric surface units and optimizing both shape and thickness to enhance isotropic stiffness. We also note the method that integrates artificial neural networks and genetic algorithm [Wang et al. 2022b] to predict and design the loading curves of shell lattices under compression.

3 Preliminary

3.1 Shell lattice

Construction. The shell lattice metamaterial is constructed by thickening a smooth periodic middle surface within the RVE. For simplicity, we consider the RVE as $Y := [-1, 1]^3$. Due to the periodic boundaries, we identify Y with a 3-torus¹ $\mathbb{T}^3 := \mathbb{R}^3 / (2\mathbb{Z})^3$. The middle surface is a closed surface embedded in \mathbb{T}^3 , denoted as $\tilde{\omega}$ (Figure 1(a)). The shell lattice, denoted as $\tilde{\Omega}^\epsilon$, is constructed by offsetting $\tilde{\omega}$ on both sides within \mathbb{T}^3 by a distance ϵ (Figure 1(b)).

Notations. We first introduce several necessary notations. We denote the contravariant (covariant) components of metric tensor on $\tilde{\omega}$ as $a^{\alpha\beta}$ ($a_{\alpha\beta}$). The second fundamental form is represented by a second-order tensor \mathbf{b} , with contravariant (covariant) components $b^{\alpha\beta}$ ($b_{\alpha\beta}$). The Christoffel symbol is denoted as $\Gamma_{\alpha\beta}^\theta$. For a vector field $\mathbf{u} : \tilde{\omega} \rightarrow \mathbb{R}^3$, we denote its tangential component as $\mathbf{u}_{\tilde{\omega}}$ and

¹Note that our derivation also applies to irregular RVE, i.e., we can define the torus as $\mathbb{R}^3 / (y_1\mathbb{Z} \times y_2\mathbb{Z} \times y_3\mathbb{Z})$ for some $y_1, y_2, y_3 > 0$, with minor changes in proof.

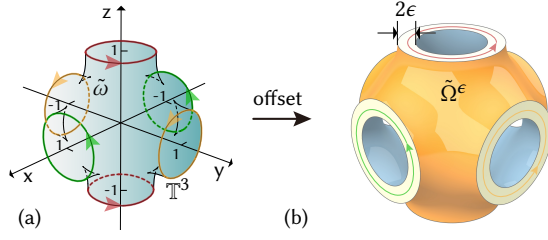


Fig. 1. (a) Due to the periodic boundaries (highlighted by colored arrows), a surface $\tilde{\omega}$ is considered as a closed surface embedded in \mathbb{T}^3 . (b) A shell lattice $\tilde{\Omega}^\epsilon$ constructed by offsetting $\tilde{\omega}$ normally on both sides.

the normal component as u_3 , i.e.,

$$\mathbf{u}_{\tilde{\omega}} = P\mathbf{u}, \quad u_3 = \mathbf{n} \cdot \mathbf{u},$$

where \mathbf{n} is the normal vector and $P = I - \mathbf{nn}^\top$ denotes the projection to the tangent space. The contravariant (covariant) components of the tangent vector $\mathbf{u}_{\tilde{\omega}}$ are denoted as u^α (u_α).

3.2 Effective stiffness

We define the effective stiffness of lattice metamaterial under a macro-strain ε as the following energy

$$E_\epsilon(\tilde{\omega}; \varepsilon) = \varepsilon : \mathbf{C}_\epsilon : \varepsilon,$$

The symbol \mathbf{C}_ϵ denotes the effective elastic tensor of the shell lattice with thickness 2ϵ . According to homogenization theory [Allaire 2002], its components are given by

$$C_\epsilon^{ijkl} = \frac{1}{|Y|} \int_{\tilde{\Omega}^\epsilon} (\varepsilon(\mathbf{u}^{ij}) + \mathbf{e}^{ij}) : \mathbf{C} : (\varepsilon(\mathbf{u}^{kl}) + \mathbf{e}^{kl}),$$

where $\mathbf{e}^{ij} = \mathbf{e}^i \otimes \mathbf{e}^j$ denotes the unit macro-strain; \mathbf{u}^{ij} is the solution of the following cell problem² when $\varepsilon = \mathbf{e}^{ij}$:

$$\arg \min_{\mathbf{u} \in \mathbf{V}_\#(\tilde{\Omega}^\epsilon)} \frac{1}{|Y|} \int_{\tilde{\Omega}^\epsilon} (\varepsilon(\mathbf{u}) + \varepsilon) : \mathbf{C} : (\varepsilon(\mathbf{u}) + \varepsilon). \quad (1)$$

Here, the function space is defined as $\mathbf{V}_\#(\tilde{\Omega}^\epsilon) := \mathbf{H}^1(\tilde{\Omega}^\epsilon) \cap \mathbf{Rig}^\perp$, where \mathbf{Rig}^\perp represents the orthogonal complement of rigid motions; the symbols $\varepsilon(\mathbf{u})$ and ε denote the strain induced by \mathbf{u} and the macro-strain, respectively; The notation \mathbf{C} signifies the elastic tensor of the base material constituting $\tilde{\Omega}^\epsilon$, with Lamé coefficients λ, μ . Note that $E_\epsilon(\tilde{\omega}; \varepsilon)$ coincides with the minimal value of the objective in (1).

4 Asymptotic analysis

We study the effective stiffness of shell lattices as the thickness tends to zero. Since it vanishes in this limit, we introduce the *asymptotic directional stiffness* (ADS) to extract the leading-order behavior, defined as

$$E_A(\tilde{\omega}; \varepsilon) := \lim_{\epsilon \rightarrow 0} \frac{E_\epsilon(\tilde{\omega}; \varepsilon)}{\rho_\epsilon(\tilde{\omega})}, \quad (2)$$

where

$$\rho_\epsilon(\tilde{\omega}) := |\tilde{\Omega}^\epsilon|/|Y|$$

is the volume fraction of the solid within RVE.

²In the literature [Panetta et al. 2017, 2015], the cell problem is also formulated as an equivalent differential equation. See the elaboration in Section 1 of the supplementary material.

Building upon the theoretical framework of [Ciarlet and Lods 1996a], we establish the convergence theorem (Theorem 1) that provides the formulation of ADS. The complete proof, which adapts key lemmas and techniques from [Ciarlet and Lods 1996a,b] to handle periodic shell structures and cell problems, is presented in the supplementary material (see also [Bernadou et al. 1994; Heby 1996] therein). We will discuss the fundamental properties of ADS in Section 4.2, where we establish its upper bound and the condition to achieve this bound (Theorem 3). As an application, this condition is used to justify the optimal bulk modulus of TPMS (Section 5).

4.1 Convergence theorem

We first introduce several notations before presenting our convergence theorem. The membrane elastic tensor $\mathbf{A}_{\tilde{\omega}}$ on $\tilde{\omega}$ is defined with components:

$$a^{\alpha\beta\theta\tau} = \lambda_0 a^{\alpha\beta} a^{\theta\tau} + \mu (a^{\alpha\theta} a^{\beta\tau} + a^{\alpha\tau} a^{\beta\theta}),$$

where $\lambda_0 = \frac{2\lambda\mu}{\lambda+2\mu}$ and $a^{\alpha\beta}$ represents the metric tensor on $\tilde{\omega}$. The membrane strain induced by a displacement field $\boldsymbol{\eta}$ on $\tilde{\omega}$ is expressed as the second-order tensor

$$\gamma(\boldsymbol{\eta}) := \text{Sym}[\nabla \boldsymbol{\eta}_{\tilde{\omega}}] - \eta_3 \mathbf{b}, \quad (3)$$

where \mathbf{b} denotes the second fundamental form and Sym denotes the symmetrization³.

REMARK 1. The membrane strain $\gamma(\boldsymbol{\eta})$ consists of two parts. The first part $\text{Sym}[\nabla \boldsymbol{\eta}_{\tilde{\omega}}]$ denotes the intrinsic stretch resulted from tangent movement $\boldsymbol{\eta}_{\tilde{\omega}}$ (blue arrows in Figure 2). The second part $(-\eta_3 \mathbf{b})$ denotes the stretch arising from normal offsetting (orange arrows in Figure 2). This contribution stems from the extrinsic curvature of $\tilde{\omega}$, which causes the normal vectors to vary spatially and become non-parallel.

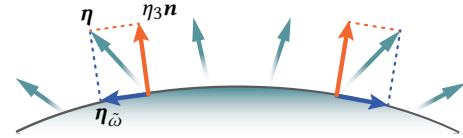


Fig. 2. Membrane strain comprises two parts: in-plane strain induced by tangent movement $\boldsymbol{\eta}_{\tilde{\omega}}$, and the stretch resulting from normal offset $\eta_3 \mathbf{n}$.

Our convergence theorem is stated as follows:

THEOREM 1. The limit in (2) is determined by

$$E_A(\tilde{\omega}; \varepsilon) = \frac{1}{|\tilde{\omega}|} \int_{\tilde{\omega}} (e_{\tilde{\omega}} + \gamma(\tilde{\mathbf{u}})) : \mathbf{A}_{\tilde{\omega}} : (e_{\tilde{\omega}} + \gamma(\tilde{\mathbf{u}})), \quad (4)$$

where $e_{\tilde{\omega}} = P\varepsilon P^\top$ is the tangential component of ε on $\tilde{\omega}$, and the vector field $\tilde{\mathbf{u}} \in \dot{\mathbf{V}}_\#(\tilde{\omega})$ solves the variational equation

$$\int_{\tilde{\omega}} \gamma(\tilde{\mathbf{u}}) : \mathbf{A}_{\tilde{\omega}} : \gamma(\mathbf{v}) = - \int_{\tilde{\omega}} e_{\tilde{\omega}} : \mathbf{A}_{\tilde{\omega}} : \gamma(\mathbf{v}) \quad \text{for all } \mathbf{v} \in \dot{\mathbf{V}}_\#(\tilde{\omega}) \quad (5)$$

in the following function space

$$\dot{\mathbf{V}}_\#(\tilde{\omega}) := \text{Completion of } (\mathbf{H}^1(\tilde{\omega}) / \ker \gamma) \text{ w.r.t. norm } |\cdot|_{\tilde{\omega}},$$

³In component form, the membrane strain is written as

$$\gamma_{\alpha\beta}(\boldsymbol{\eta}) := \frac{1}{2} (\partial_\alpha \eta_\beta + \partial_\beta \eta_\alpha) - \Gamma_{\alpha\beta}^\theta \eta_\theta - b_{\alpha\beta} \eta_3.$$

where the norm $|\cdot|_{\tilde{\omega}}$ is given by

$$|\mathbf{v}|_{\tilde{\omega}} := \left(\int_{\tilde{\omega}} \gamma(\mathbf{v}) : \mathbf{A}_{\tilde{\omega}} : \gamma(\mathbf{v}) \right)^{1/2}.$$

REMARK 2. The notation $\ker \gamma$ signifies the kernel of strain γ , which consists of displacements that induce zero membrane strain. This space is also termed as inextensional displacements in the literature.

The detailed proof is elaborated in SM Section 4.1. Since the solution $\tilde{\mathbf{u}}$ of (5) is linearly dependent on the macro-strain ε , the ADS admits the following compact form

$$E_A(\tilde{\omega}; \varepsilon) = \varepsilon : \mathbf{C}_A : \varepsilon, \quad (6)$$

where \mathbf{C}_A is termed as the *asymptotic elastic tensor*, with components given by

$$C_A^{ijkl} := \frac{1}{|\tilde{\omega}|} \int_{\tilde{\omega}} (\gamma(\tilde{\mathbf{u}}^{ij}) + \mathbf{e}_{\tilde{\omega}}^{ij}) : \mathbf{A}_{\tilde{\omega}} : (\gamma(\tilde{\mathbf{u}}^{kl}) + \mathbf{e}_{\tilde{\omega}}^{kl}). \quad (7)$$

Here, $\tilde{\mathbf{u}}^{ij}$ is the solution of (5) for $\varepsilon = \mathbf{e}^{ij}$ and $\mathbf{e}_{\tilde{\omega}}^{ij} = \mathbf{P} \mathbf{e}^{ij} \mathbf{P}^T$ represents the tangential component.

4.2 The upper bound of ADS

By substituting the variational equation (5) into (4) with $\mathbf{v} = \tilde{\mathbf{u}}$, the ADS can be expressed as (Appendix A)

$$E_A(\tilde{\omega}; \varepsilon) = E_M(\tilde{\omega}; \varepsilon) - \frac{1}{|\tilde{\omega}|} \int_{\tilde{\omega}} \gamma(\tilde{\mathbf{u}}) : \mathbf{A}_{\tilde{\omega}} : \gamma(\tilde{\mathbf{u}}). \quad (8)$$

We define $E_M(\tilde{\omega}; \varepsilon)$ as the *homogeneous membrane energy*, given by

$$E_M(\tilde{\omega}; \varepsilon) := \varepsilon : \bar{\mathbb{P}} : \varepsilon, \quad (9)$$

where $\bar{\mathbb{P}} := \frac{1}{|\tilde{\omega}|} \int_{\tilde{\omega}} \mathbb{P}$ represents the average of the fourth-order tensor \mathbb{P} over $\tilde{\omega}$, defined as

$$[\mathbb{P}]^{ijkl} = \lambda_0 P^{ij} P^{kl} + \mu (P^{il} P^{jk} + P^{ik} P^{jl}). \quad (10)$$

The detailed derivation is provided in Appendix A. Since $\mathbf{A}_{\tilde{\omega}}$ is a positive definite tensor, we have $\frac{1}{|\tilde{\omega}|} \int_{\tilde{\omega}} \gamma(\tilde{\mathbf{u}}) : \mathbf{A}_{\tilde{\omega}} : \gamma(\tilde{\mathbf{u}}) \geq 0$ with equality holding if and only if $\tilde{\mathbf{u}} = \mathbf{0}$. This leads to the following theorem that establishes the upper bound of $E_A(\tilde{\omega}; \varepsilon)$.

THEOREM 2. The asymptotic directional stiffness satisfies

$$E_A(\tilde{\omega}; \varepsilon) \leq E_M(\tilde{\omega}; \varepsilon),$$

and the equality holds if and only if (5) admits a zero solution.

REMARK 3. The intuition behind this theorem is as follows: When the surface is subjected to a macro-strain ε , the energy E_M corresponds to the strain energy under purely affine deformation. However, due to the presence of void space around the surface within the RVE, the surface can further relax, reducing the energy to the final value E_A . If no relaxation occurs (i.e., $\tilde{\mathbf{u}} = \mathbf{0}$), then the final stable energy E_A equals E_M . See Figure 3 for an illustration.

REMARK 4. Although E_M still depends on ε as does E_A , it has a simpler structure since the ‘matrix’ $\bar{\mathbb{P}}$ of the quadratic form (9) only depends on the normal vector distribution of $\tilde{\omega}$, facilitating analysis. For example, we know the eigenvalues of tensor $\bar{\mathbb{P}}$ sum to $2\lambda_0 + 6\mu$, namely,

$$\frac{1}{6} \sum_{i=1}^6 \lambda_i(E_M) = \frac{1}{3} \lambda_0 + \mu,$$

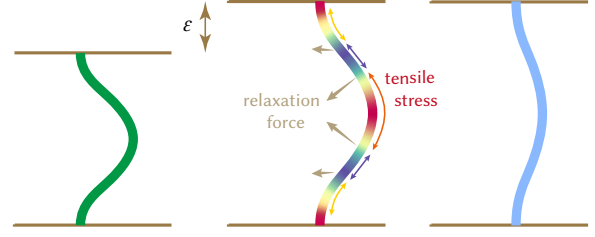


Fig. 3. Section view of surface deformation under a macroscopic stretch ε along the z -axis. Left: undeformed surface. Middle: the RVE and surface undergo affine deformation, resulting in strain energy (E_M). The projected in-plane strain varies across the surface, leading to non-uniform tensile stress whose divergence induces a relaxation force. Right: the surface relaxes under this force to reach a lower energy state (E_A).

where λ_i denotes the i -th eigenvalue. See the proof in Appendix B. This result implies that while E_M varies with ε , its average eigenvalue is constant.

4.3 Achieving the upper bound of ADS

One common objective in lattice metamaterial design is stiffness optimization [Liu et al. 2024; Ma et al. 2021], motivating our search for surfaces achieving the upper bound E_M . While Theorem 2 characterizes the optimal condition, its direct application as a design criterion is impractical due to the need to solve variational equation (5). Therefore, we introduce an equivalent necessary and sufficient condition:

THEOREM 3. The asymptotic directional stiffness satisfies

$$E_A(\tilde{\omega}; \varepsilon) \leq E_M(\tilde{\omega}; \varepsilon),$$

and the equality holds if and only if the following relations hold over $\tilde{\omega}$:

$$\begin{aligned} (2(\lambda_0 + \mu) \mathbf{b} + 4\mu \mathbf{HP}) \varepsilon \cdot \mathbf{n} &= \mathbf{0} \\ 2(\lambda_0 \mathbf{HP} + \mu \mathbf{b}) : \varepsilon &= \mathbf{0}, \end{aligned} \quad (11)$$

where the second fundamental form is considered as a tensor in \mathbb{T}^3 during the contraction⁴.

REMARK 5. The tangent vector and scalar on the LHS of (11) are exactly the tangential and normal components of the relaxation force acting on the surface, as shown in Figure 3.

The complete proof of Theorem 3 is provided in SM Section 4.2. Note that this condition only involves the geometry of the middle surface without solving any equation. It suggests that constructing a surface satisfying (11) universally for all ε would yield a optimal (in the sense of stiffness) middle surface for designing shell lattice. Unfortunately, we have the following theorem

THEOREM 4. The only smooth surface such that (11) holds everywhere for every ε is plane.

PROOF. Suppose $\tilde{\omega}$ satisfies (11) at every point for every ε , then we have

$$2(\lambda_0 \mathbf{HP} + \mu \mathbf{b}) = \mathbf{0}. \quad (12)$$

It follows that

$$\text{tr } 2(\lambda_0 \mathbf{HP} + \mu \mathbf{b}) = (4\lambda_0 + 2\mu) H = \mathbf{0},$$

⁴This is feasible as $\tilde{\omega}$ is smoothly embedded in \mathbb{T}^3 .

where we have utilized (35) and the identity $\text{tr } \mathbf{b} = 2H$. The above equation implies zero mean curvature: $H = 0$. Hence we have $\mathbf{b} = \mathbf{0}$ according to (12). This means $\tilde{\omega}$ is a plane in \mathbb{T}^3 . \square

Nevertheless, non-trivial surfaces that achieve the upper bound exist if we only consider certain strain, as we will show in the next section.

5 The optimal asymptotic bulk modulus of TPMS

We define the *asymptotic bulk modulus* (ABM) as the ADS under the hydrostatic strain ($\varepsilon = \frac{1}{3}I$), i.e.,

$$K_A(\tilde{\omega}) := E_A(\tilde{\omega}; \frac{1}{3}I).$$

Theorem 2 gives the following upper bound on ABM:

$$K_A(\tilde{\omega}) \leq E_M(\tilde{\omega}; \frac{1}{3}I).$$

Surprisingly, we have the following proposition

PROPOSITION 1. *The homogeneous membrane energy under hydrostatic loading is constant:*

$$E_M(\tilde{\omega}; \frac{1}{3}I) = \frac{4}{9}(\lambda_0 + \mu).$$

PROOF. Direct computation shows

$$\begin{aligned} E_M(\tilde{\omega}; \frac{1}{3}I) &= \frac{1}{9|\tilde{\omega}|} \int_{\tilde{\omega}} I : \mathbb{P} : I = \frac{1}{9|\tilde{\omega}|} \int_{\tilde{\omega}} \lambda_0 (\text{tr } P)^2 + 2\mu \text{tr } PP^\top \\ &= \frac{1}{9|\tilde{\omega}|} \int_{\tilde{\omega}} 4(\lambda_0 + \mu) = \frac{4}{9}(\lambda_0 + \mu), \end{aligned}$$

where we have used (10) and (35). \square

The interesting problem is which kind of surface attains this upper bound. If we substitute $\varepsilon = \frac{1}{3}I$ into LHS of (11), we get

$$\begin{aligned} (2(\lambda_0 + \mu)\mathbf{b} + 4\mu HP) \varepsilon \cdot \mathbf{n} &\rightarrow \mathbf{0} \\ 2(\lambda_0 HP + \mu\mathbf{b}) : \varepsilon &\rightarrow \frac{4}{3}(\lambda_0 + \mu)H. \end{aligned} \quad (13)$$

Here, the first relation holds because \mathbf{b} and P are both orthogonal to the normal vector; the second utilized (35) and the identity $\text{tr } \mathbf{b} = 2H$. Therefore, the optimality condition (11) reduces to $H = 0$ in this case. Consequently, we have derived the following theorem.

THEOREM 5. *The asymptotic bulk modulus satisfies*

$$K_A(\tilde{\omega}) \leq \frac{4}{9}(\lambda_0 + \mu), \quad (14)$$

and the equality holds if and only if $\tilde{\omega}$ is TPMS.

REMARK 6. *As discussed in Remark 5, equation (13) implies that the relaxation force under hydrostatic loading is a normal force proportional to the mean curvature. Therefore, if the mean curvature vanishes, no relaxation occurs, and the ADS reaches its upper bound.*

Relation to Hashin-Shtrikman bound. This theorem explains the exceptionally high bulk modulus observed in TPMS shell lattice metamaterials [Chen et al. 2019; Deng and Cheng 2021; Wang et al. 2022c], which approaches the Hashin-Shtrikman (HS) upper bound [Hashin and Shtrikman 1963]. Here, we show how the theorem relates to this bound. According to the composite material theory, the HS upper bound for bulk modulus is given by

$$K^{HS}(\rho) := \frac{4\rho\mu(3\lambda + 2\mu)}{12\mu + (1 - \rho)(9\lambda + 6\mu)},$$

where ρ is the volume fraction of the material within the unit cell. When this bound applies to our problem, we immediately get

$$E_\varepsilon(\tilde{\omega}; \frac{1}{3}I) = K(\tilde{\Omega}^\varepsilon) \leq K^{HS}(\rho(\tilde{\Omega}^\varepsilon)). \quad (15)$$

If we divide $\rho(\tilde{\Omega}^\varepsilon)$ on both sides of (15) and let $\varepsilon \rightarrow 0$, we have

$$\limsup_{\varepsilon \rightarrow 0} \frac{E_\varepsilon(\tilde{\omega}; \frac{1}{3}I)}{\rho(\tilde{\Omega}^\varepsilon)} \leq \lim_{\varepsilon \rightarrow 0} \frac{K^{HS}(\rho(\tilde{\Omega}^\varepsilon))}{\rho(\tilde{\Omega}^\varepsilon)} = \frac{dK^{HS}}{d\rho}(0) = \frac{4}{9}(\lambda_0 + \mu),$$

which is exactly the upper bound in (14). However, this derivation necessitates that the lattice metamaterial exhibits cubic symmetry; otherwise, the HS bound does not generally hold. Our approach relaxes this constraint, provided that the shell lattice has a smooth, periodic middle surface. As a result, this theorem implies that any cubic TPMS shell lattice consistently exhibits a bulk modulus close to HS upper bound (at low volume fractions). Even when the surface lacks cubic symmetry, this theorem remains valid, though the HS bound may no longer apply. We stress that (14) holds even when the surface is not closed or the thickness is not uniform (SM Section 4.3).

6 Discretization and optimization

The optimality condition (11) in Theorem 3 offers a guiding principle for designing surfaces with extreme stiffness. However, constructing a surface that satisfies (11) everywhere for an arbitrary strain is not straightforward, except in the special case of bulk modulus. Moreover, the upper bound itself depends on the surface geometry, potentially limiting the achievable stiffness. To address these issues, we introduce a numerical framework for optimizing ADS. We first illustrate our discretization scheme for evaluating ADS (Section 6.1) before presenting the optimization algorithm (Section 6.2).

6.1 Discretization of ADS

We approximate the middle surface $\tilde{\omega}$ by a triangular mesh, denoted as \mathcal{M} . The sets of faces, edges, and vertices of \mathcal{M} are denoted as \mathcal{F} , \mathcal{E} , and \mathcal{V} , respectively.

6.1.1 The membrane strain. By definition, $\gamma(\mathbf{u})$ is the change of metric when $\tilde{\omega}$ deforms along a vector field \mathbf{u} . Thus, a direct approximation computes the strain of each triangular face $\Delta \mathbf{x}_1 \mathbf{x}_2 \mathbf{x}_3$ under vertex displacements \mathbf{u}_i ($i = 1, 2, 3$) as

$$\gamma(\mathbf{u}) \approx \text{Sym}[\nabla(P_f \mathbf{u})], \quad (16)$$

where P_f denotes the projection onto face f . Essentially, this is a plane stress element with no bending effects taken into account. The approximation, however, results in a highly fluctuating displacement solution of (5), which is physically implausible (Figure 5 middle).

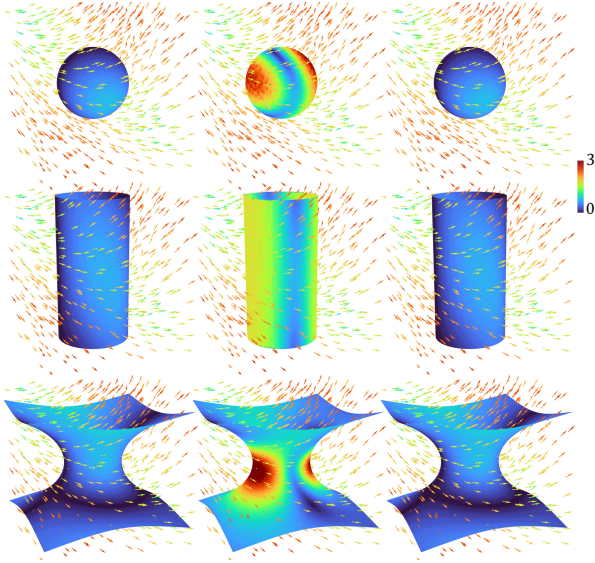


Fig. 4. Approximation error of the membrane strain on elliptic, parabolic, and hyperbolic surfaces under a smooth vector field $(\cos(x), \sin(xy), \sin(x+z))$ (visualized with colored arrows). Left : the plane stress element (16). Middle : scheme (18). Right : scheme (19).

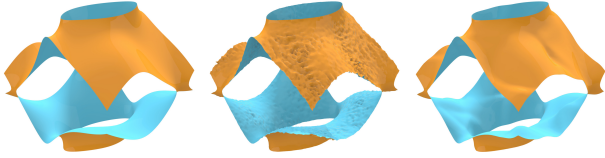


Fig. 5. Deformation solved from (5) under hydrostatic loading ($\varepsilon = \frac{1}{3}I$) with different elements. Left : the input surface. Middle : plane stress element (16). Right : scheme (19).

As suggested by the definition (3) of $\gamma(\mathbf{u})$, this issue may stem from the lack of curvature information in the surface. To address this, we attempt to approximate the second fundamental form to better capture the surface's geometry.

Approximating the second fundamental form. We apply finite difference scheme [Rusinkiewicz 2004] to approximate the second fundamental form. According to the definition, we have

$$\mathbf{b}(\mathbf{l}_{ij}, \mathbf{l}_{ij}) = -(\mathbf{n}_j - \mathbf{n}_i) \cdot \mathbf{l}_{ij}, \quad (17)$$

where \mathbf{n}_i denotes the normal at i -th vertex, computed using the angle based weighting scheme, and $\mathbf{l}_{ij} = \mathbf{v}_j - \mathbf{v}_i$ denotes the edge vector. On each face $f \in \mathcal{F}$, we approximate \mathbf{b} by a symmetric matrix $\mathbf{b}_f \in \mathbb{R}^{2 \times 2}$ with three independent components determined from its evaluation (17) over the edge vectors of the face. On the other hand, the normal displacement u_3 within the face is approximated by linear interpolation from the displacements at the vertices:

$$u_3 = \sum_{i=1}^3 \phi_i \mathbf{u}_i \cdot \mathbf{n}_i,$$

where ϕ_i denotes the barycentric coordinate. Thus, we refine our approximation of the membrane strain as follows:

$$\gamma(\mathbf{u})|_f \approx \text{Sym}[\nabla(P_f \mathbf{u})] - u_3 \mathbf{b}_f. \quad (18)$$

Unfortunately, this formulation exhibits poor accuracy in experiments (Figure 4 middle). We find that this significant error actually stems from the symmetric gradient in (18), instead of the second fundamental form.

Correction of tangent strain. To illustrate this issue, we consider the approximation of a curved triangular surface patch by a planar triangular face (Figure 6). We assume that the vertex positions and normals coincide (blue arrows in Figure 6), and that the curvature is small relative to the dimensions of both patches. In this case, the tangent space of the surface can be well approximated by the plane of the triangle, along with the tangent vectors defined on it. However, this approximation is in the sense of L^2 norm. Therefore, it is not accurate to approximate the gradient of the tangent vectors by differentiating this L^2 approximation, as (18) does. To address this issue, we must account for the curvature of the surface, which is characterized by the non-parallel vertex normals.

This observation inspires us to use per-vertex projection instead of a uniform projection (P_f) to extract the tangential component. In practice, we first rotate the vertex tangent space to align with the plane of the face before projecting the displacement (Figure 6). Then we approximate the tangent vector within the face as the linear interpolation of the projected ones at the vertices:

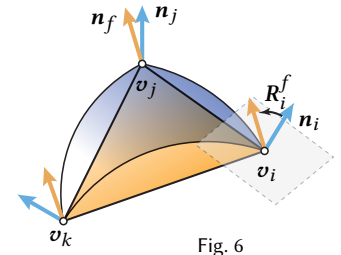


Fig. 6

$$\mathbf{u}_\tau = \sum_{i=1}^3 \phi_i P_f R_i^f \mathbf{u}_i,$$

where ϕ_i denotes barycentric coordinate, and R_i^f is a rotation matrix aligning vertex normal \mathbf{n}_i to face normal \mathbf{n}_f (yellow arrows in Figure 6). Finally, our improved approximation is given by

$$\gamma(\mathbf{u})|_f \approx \text{Sym}[\nabla \mathbf{u}_\tau] - u_3 \mathbf{b}_f. \quad (19)$$

The numerical experiments demonstrate a significant improvement in accuracy after this correction (Figure 4 right).

Although the plane stress element (16) and our scheme exhibit comparable accuracy in discretizing the strain w.r.t. a smooth vector field (Figure 4 left and right), our approach yields a more convincing solution to (5) (Figure 5 right). The accuracy and convergence rate of this scheme are further investigated in Section 7.4.

6.1.2 Solve for ADS. With the discretized membrane strain, the variational equation (5) is converted into the following linear system (Appendix C):

$$\mathbf{K}^h \mathbf{u}^h = \mathbf{f}^h, \quad (20)$$

where \mathbf{K}^h denotes the global stiffness matrix, and \mathbf{f}^h is the force vector assembled from the macro-strain ε . The vector \mathbf{u}^h consists of the vertex displacements that we solve for. We denote the force

vector as \mathbf{f}_{ij}^h when $\varepsilon = \mathbf{e}^{ij}$, with the corresponding solution of (20) denoted as \mathbf{u}_{ij}^h . Finally, the components of asymptotic elastic tensor are computed as:

$$C_A^{ijkl} = E_M^h(\mathbf{e}^{ij}, \mathbf{e}^{kl}) - \frac{\mathbf{u}_{ij}^h \cdot \mathbf{f}_{kl}^h}{\text{Area}(M)}, \quad (21)$$

where

$$E_M^h(\mathbf{e}^{ij}, \mathbf{e}^{kl}) := \frac{1}{\text{Area}(M)} \sum_{\hat{f} \in \mathcal{F}} \int_{\hat{f}} \mathbf{A}_{\hat{\omega}} : P_f \mathbf{e}^{ij} P_f^\top : P_f \mathbf{e}^{kl} P_f^\top.$$

We have used the variational equation (5) to derive (21), similar to (8).

6.2 Shape optimization

As shown in the definition of membrane strain, computing the second fundamental form and the Christoffel symbols requires second-order derivatives of the surface's embedding. Although it can be approximated piecewise (Section 6.1.1), the shape sensitivity involves third-order derivatives, which makes computation on a triangular mesh challenging. While higher-order geometric representations such as NURBS or Bézier patches can address this issue, their generation and optimization on a periodic surface with complex topology is non-trivial. To overcome this challenge, we leverage the variational equation (5) to eliminate the higher-order terms, resulting in a feasible formulation that is easier to discretize (Section 6.2.1). This sensitivity is then used to derive a gradient-based flow for optimizing ADS (Section 6.2.3).

6.2.1 Sensitivity of ADS. As tangential movement does not change the surface shape, we assume that $\tilde{\omega}$ evolves under a normal velocity $v_n : \tilde{\omega} \rightarrow \mathbb{R}$. The time derivative of ADS, which by formulation (4) is a ratio of an integral (denoted as I_a^s) to the surface area (denoted as A), takes the following form

$$\dot{E}_A = \frac{\dot{I}_a^s}{A} - \frac{I_a^s \dot{A}}{A^2}. \quad (22)$$

The change of area is straightforward to compute, given by

$$\dot{A} := - \int_{\tilde{\omega}} 2v_n H. \quad (23)$$

The discretization of this integral is discussed in Appendix D. Then it remains to compute the time derivative of the integral \dot{I}_a^s .

The vanilla derivation gives the following time derivative (SM Section 8):

PROPOSITION 2. *The time derivative \dot{I}_a^s is given by*

$$\begin{aligned} \dot{I}_a^s &= \int_{\tilde{\omega}} 2v_n (\gamma(\tilde{\mathbf{u}}) + e_{\tilde{\omega}}) : (\mathbf{B} - H\mathbf{A}_{\tilde{\omega}}) : (\gamma(\tilde{\mathbf{u}}) + e_{\tilde{\omega}}) \\ &+ \int_{\tilde{\omega}} 2(\gamma(\tilde{\mathbf{u}}) + e_{\tilde{\omega}}) : \mathbf{A}_{\tilde{\omega}} : \xi(\tilde{\mathbf{u}}), \end{aligned} \quad (24)$$

where \mathbf{B} is a fourth-order tensor defined as

$$B^{ijkl} := \lambda_0(b^{\alpha\beta} a^{\theta\tau} + a^{\alpha\beta} b^{\theta\tau}) + \mu(b^{\alpha\theta} a^{\beta\tau} + a^{\alpha\theta} b^{\beta\tau} + b^{\alpha\tau} a^{\beta\theta} + a^{\alpha\tau} b^{\beta\theta}), \quad (25)$$

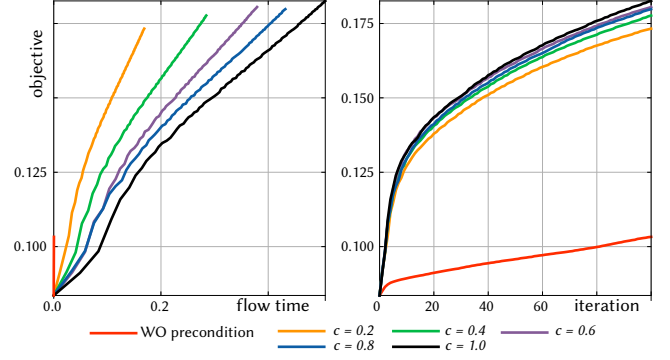


Fig. 7. Maximizing ADS under strain \mathbf{e}^{33} without precondition and with different precondition strength parameter c . The left and right plots show the objective change w.r.t. the flow time (parameter t in (29)) and the iteration, respectively. Although the objective evolves fastest w.r.t. flow time without preconditioning (left), the total clock time required to reach the same objective value depends on the number of iterations, which is significantly reduced after preconditioning (right).

and $\xi(\tilde{\mathbf{u}})$ is a second-order tensor, defined as

$$\begin{aligned} \xi(\mathbf{u}) &:= v_n \tilde{\mathbf{u}}_{\tilde{\omega}} \cdot \nabla \mathbf{b} + 2\text{Sym}[\mathbf{b} \tilde{\mathbf{u}}_{\tilde{\omega}} \nabla v_n^\top] - (\nabla v_n \cdot \tilde{\mathbf{u}}_{\tilde{\omega}}) \mathbf{b} \\ &- \tilde{u}_3 (\nabla^2 v_n - v_n \mathbf{c}) + 2\text{Sym}[P \varepsilon n \nabla v_n^\top]. \end{aligned}$$

where $\mathbf{c} = \mathbf{b} \cdot \mathbf{b}$ denotes the third fundamental form.

A challenge with this formulation is the presence of the covariant derivative of the second fundamental form ($\nabla \mathbf{b}$) and the second-order derivative ($\nabla^2 v_n$), both of which are difficult to evaluate on a discrete mesh. While the existing work [Rusinkiewicz 2004] proposed an approximation for the curvature derivatives on discrete meshes, we introduce a more refined approach that bypasses this approximation.

Eliminate the higher-order derivatives. To handle this problem, we notice that both terms can be written as

$$\begin{aligned} v_n \tilde{\mathbf{u}}_{\tilde{\omega}} \cdot \nabla \mathbf{b} &= \nabla(v_n \mathbf{b} \tilde{\mathbf{u}}_{\tilde{\omega}}) - \mathbf{b} \nabla(v_n \tilde{\mathbf{u}}_{\tilde{\omega}}) \\ \tilde{u}_3 \nabla^2 v_n &= \nabla(\tilde{u}_3 \nabla v_n) - \nabla \tilde{u}_3 \nabla v_n^\top. \end{aligned}$$

The benefit is that we can leverage the variational equation (5) to eliminate both terms by substituting the test function with $\mathbf{v} = v_n \mathbf{b} \tilde{\mathbf{u}}_{\tilde{\omega}}$ (resp. $\tilde{u}_3 \nabla v_n$). Similarly, the term $(\nabla v_n \cdot \tilde{\mathbf{u}}_{\tilde{\omega}}) \mathbf{b}$ is eliminated by letting $\mathbf{v}_3 = (\nabla v_n \cdot \tilde{\mathbf{u}}_{\tilde{\omega}})$ and $\mathbf{v}_{\tilde{\omega}} = \mathbf{0}$.

REMARK 7. *A potential issue is that the substituted test functions may not belong to the space $\dot{V}_{\#}(\tilde{\omega})$, particularly those involving $\tilde{\mathbf{u}}_{\tilde{\omega}}$. As a result, the above approach implicitly assumes sufficient regularity of both the solution $\tilde{\mathbf{u}}$ and the normal velocity v_n .*

After collecting the remaining terms, we can replace $\xi(\tilde{\mathbf{u}})$ in (24) with

$$\zeta(\tilde{\mathbf{u}}) := \mathbf{b} \tilde{\mathbf{u}}_{\tilde{\omega}} \nabla v_n^\top - v_n \mathbf{b} \nabla \tilde{\mathbf{u}}_{\tilde{\omega}} + \nabla \tilde{u}_3 \nabla v_n^\top + \tilde{u}_3 v_n \mathbf{c} + 2P \varepsilon n \nabla v_n^\top, \quad (26)$$

where we omit the symmetrization operation for brevity, as its contracted tensor in (24) is symmetric. Thus, we propose the following improved sensitivity formulation

PROPOSITION 3. The time derivative \dot{I}_a^s is evaluated as

$$\begin{aligned} \dot{I}_a^s &= \int_{\tilde{\omega}} 2v_n (\gamma(\tilde{\mathbf{u}}) + \mathbf{e}_{\tilde{\omega}}) : (\mathbf{B} - H\mathbf{A}_{\tilde{\omega}}) : (\gamma(\tilde{\mathbf{u}}) + \mathbf{e}_{\tilde{\omega}}) \\ &+ \int_{\tilde{\omega}} 2(\gamma(\tilde{\mathbf{u}}) + \mathbf{e}_{\tilde{\omega}}) : \mathbf{A}_{\tilde{\omega}} : \zeta(\tilde{\mathbf{u}}), \end{aligned}$$

where \mathbf{B} is defined in (25) and $\zeta(\tilde{\mathbf{u}})$ is defined in (26).

This new formulation contains no higher-order derivatives, resulting in a suitable discretization on a triangle mesh (Appendix 6.1).

6.2.2 *Sensitivity of asymptotic elastic tensor.* Since ADS is a quadratic form, we can derive the sensitivity of its associated matrix, the asymptotic elastic tensor C_A , based on the sensitivity of its evaluation on strains. Alternatively, one may directly compute the time derivative of the integral in the definition (7), following a similar procedure as in Section 6.2.1. Both approaches lead to the same result, summarized below:

PROPOSITION 4. The time derivative of asymptotic elastic tensor C_A is given by

$$\dot{C}_{ijkl}^s = \frac{\dot{I}_{ijkl}^s}{A} - \frac{I_{ijkl}^s \dot{A}}{A^2}, \quad (27)$$

where I_{ijkl}^s denotes the integral in (7), respectively; and their time derivatives are

$$\begin{aligned} \dot{I}_{ijkl}^s &= \int_{\tilde{\omega}} 2v_n (\gamma(\tilde{\mathbf{u}}^{ij}) + \mathbf{e}_{\tilde{\omega}}^{ij}) : (\mathbf{B} - H\mathbf{A}_{\tilde{\omega}}) : (\gamma(\tilde{\mathbf{u}}^{kl}) + \mathbf{e}_{\tilde{\omega}}^{kl}) \\ &+ \int_{\tilde{\omega}} (\gamma(\tilde{\mathbf{u}}^{ij}) + \mathbf{e}_{\tilde{\omega}}^{ij}) : \mathbf{A}_{\tilde{\omega}} : \zeta(\tilde{\mathbf{u}}^{kl}) \\ &+ \int_{\tilde{\omega}} (\gamma(\tilde{\mathbf{u}}^{kl}) + \mathbf{e}_{\tilde{\omega}}^{kl}) : \mathbf{A}_{\tilde{\omega}} : \zeta(\tilde{\mathbf{u}}^{ij}). \end{aligned}$$

The derivation follows the same spirit in Section 6.2.1 with minor changes in the integrand, and is therefore omitted here.

6.2.3 *Optimization.* According to (23), (22), and (24), the time derivative \dot{I}_A^s is a linear functional of the normal velocity v_n . Hence, we can define the L^2 gradient $\text{grad } I_A^s$ such that

$$\dot{I}_A^s(v_n) = \langle \text{grad } I_A^s, v_n \rangle_{L^2(\tilde{\omega})}, \quad (28)$$

and then performing a gradient descent flow as

$$\frac{d\tilde{\omega}}{dt} = -\text{grad } I_A^s. \quad (29)$$

However, the Armijo condition during line search forces a significant reduction in the time step when using the L^2 gradient, resulting in very small time steps even if a large initial step is specified, thereby slowing down the optimization (Figure 7 right). Similar issues are also noted in [Yu et al. 2021a,b], where they are addressed by using the gradient derived from fractional Sobolev inner product that matches the energy objective. Here, we resort to another approach. We precondition this gradient with the Laplacian

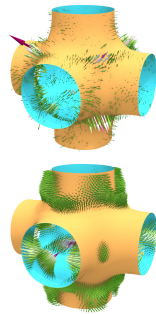


Fig. 8

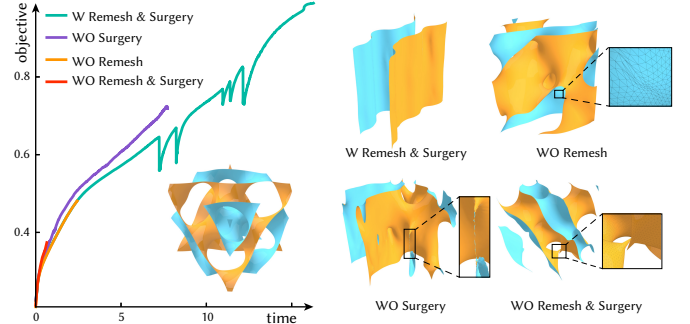


Fig. 9. Maximizing ADS objective C_A^{3333} with/without remeshing and surgery operations. The input surface is shown in the left inset. The decrease in the objective is observed due to either the surgery operation or failure of the line search (WO surgery). Without remeshing or surgery, the optimization stagnates because of poor mesh quality or the formation of necking singularities (right inset).

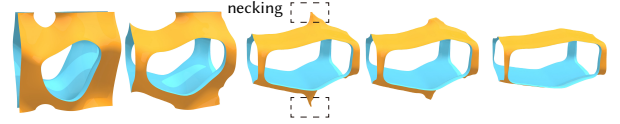


Fig. 10. A necking singularity emerges when maximizing the stiffness under shear strain \mathbf{e}^{12} . The surface escapes this configuration through numerical surgery.

operator by solving for a modified gradient d_n from the following equation

$$(Id - c\Delta)d_n = -(c+1)\text{grad } I_A,$$

where Id denotes the identity map, Δ denotes the Laplacian operator, and c is a positive constant controlling the strength of the preconditioning⁵ (typically $c = 1$). Since the operator $(Id - c\Delta)$ is positive definite, the preconditioned gradient (Figure 8 bottom) is still a descent direction. While the change of the objective becomes slower w.r.t. flow time⁶ (Figure 7 left), much larger time steps are allowed during line search, thus accelerating the optimization w.r.t. iteration times (Figure 7 right).

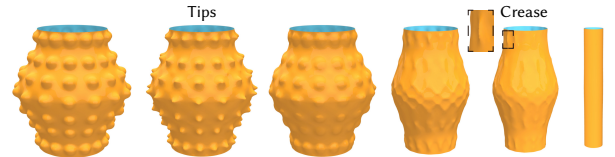


Fig. 11. Tips and creases appear when maximizing Young's modulus along the z -axis, and are removed by surgery operations. The input and optimized surfaces are shown on the left and right, respectively.

In the discrete setting, we approximate $\text{grad } I_A$ by a vector V^h , assembled from the coefficients of per-vertex normal velocities (v_n^i)

⁵When $c = 0$ and ∞ , the preconditioned gradient is the L^1 and H^1 gradient, respectively.

⁶Here, flow time refers to the time variable (t) in (29), not the wall-clock time.

Algorithm 1: Armijo line search

Input: Objective f , step vector d_n , gradient g_n
Output: Time step Δt .

```

1  $\alpha \leftarrow 0.1, \tau \leftarrow 0.7;$ 
2  $\Delta t \leftarrow \text{AdaptiveTimeStep}();$ 
3 for  $i \leftarrow 0$  to  $\text{max\_iter}$  do
4   if  $f(\mathcal{V} + \Delta t d_n) < f(\mathcal{V}) + \alpha \Delta t d_n^\top g_n$  then Output  $\Delta t;$ 
5    $\Delta t \leftarrow \tau \Delta t;$ 
6 end
7 Output  $\Delta t;$ 

```

Algorithm 2: Shape optimization for asymptotic properties

Input: Periodic mesh \mathcal{M} , objective f ;
Output: Optimized mesh.

```

1  $i \leftarrow 0;$ 
2  $\text{converged} \leftarrow \text{false};$ 
3 while  $! \text{converged} \ \&\& \ i < \text{max\_iter}$  do
4   if  $i \% 4 == 0$  then
5      $\mathcal{M} \leftarrow \text{NumericalSurgery}(\mathcal{M});$ 
6   end
7    $\mathcal{M} \leftarrow \text{DynamicRemesh}(\mathcal{M});$ 
8   Assemble and solve equation (20);
9   Evaluate ADS tensor  $C_A$ ; // Section 6.1.2
10  Evaluate objective  $f^i$ ;
11  Evaluate the  $L^2$  gradient  $g_n$  based on (31), (28), and (27);
12  Solve for preconditioned gradient  $d_n$  from (30);
13   $\Delta t \leftarrow \text{ArmijoLineSearch}(f, g_n, d_n);$  // Alg. 1
14   $\mathcal{V} \leftarrow \mathcal{V} + \Delta t d_n;$ 
15   $\text{converged} \leftarrow \text{CheckConvergence}(f^i, \Delta t);$ 
16   $i \leftarrow i + 1;$ 
17 end
18 Output  $\mathcal{M};$ 

```

in the discretized form of (22) (Appendix D). We then solve for the preconditioned gradient d^h from the following equation

$$(\mathbf{M} - c\mathbf{L})d^h = -(c+1)V^h, \quad (30)$$

where \mathbf{M} denotes the mass matrix and \mathbf{L} is the cotangent Laplacian matrix. Finally, we update the vertex positions by

$$x_i^{k+1} = x_i^k + \Delta t d_i^h, \quad \forall i \in \mathcal{V},$$

where Δt is a time step, determined using Armijo line search (Alg.1). We consider the optimization as converged when either the time step is less than 10^{-4} for five consecutive iterations, or the time derivative of the objective, approximated by the slope of a linear regression fit to the history of the last 50 iterations, is less than 10^{-3} .

Adaptive initial time step. During the line search, each evaluation of objective requires solving equation (20), which is time consuming. A large initial time step leads to excessive backtracking steps and increased equation solves. To reduce the overhead, we set the initial step in the Armijo line search as the average of those determined in

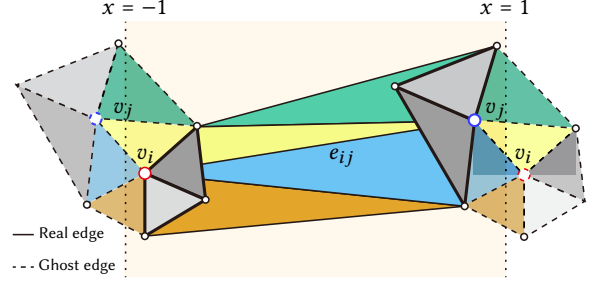


Fig. 12. Reproduced 1-ring of vertex (v_i and v_j) when the incident edge is longer than a threshold.

the last five iterations, multiplied by a factor of 2 to avoid reducing the time step to zero.

Dynamic remesh. As the mesh quality degrades during the flow, the optimization eventually stalls due to the increasingly small time step, even with the preconditioned gradient. To address this, we employ the dynamic remeshing algorithm proposed in [Yu et al. 2021a]. We refer readers to Section 6 in [Yu et al. 2021a] for implementation details. With the remeshing procedure in place, the optimization proceeds normally, see the comparison in Figure 9.

Numerical surgery. As the optimization progresses, the surface may develop necking singularities (Figure 10). Inspired by [Kovács 2024], we apply a numerical surgery procedure to remove them. We identify candidate regions based on the maximal principal curvature, the triangles with vertex curvature values larger than a threshold (typically 25) are selected and grouped into connected components. For each component, we first remove its constituent triangles and fill the resulting hole using the CGAL [Hemmer 2024] library, then a bi-Laplacian fairing step [Botsch and Kobbelt 2004] is performed in the k -ring of the filling patch, where $k = 4$ in our experiments. This procedure also eliminates undesired tips and creases that may arise during the optimization (Figure 11). See also the ablation study in Figure 9. To reduce the computational overhead, this operation is performed every four iterations.

6.2.4 Custom objective. With above techniques, we can optimize a custom objective function $f(C_A)$, with sensitivity given by

$$\frac{d}{dt} f = \frac{\partial f}{\partial C_A^{ijkl}} \dot{C}_A^{ijkl}, \quad (31)$$

where we adopted the convention of Einstein summation. The gradient evaluation and optimization steps remain the same as before. Pseudocodes of our overall optimization pipeline are shown in Alg. 2.

7 Validation of theory

In this section, we first illustrate our method for generating and handling periodic surfaces (Section 7.1 and 7.2). Then we conduct numerical experiments in Section 7.4 to verify the convergence of ADS formula (2) and assess the accuracy of our discretization scheme. In Section 7.5, we validate the optimality of TPMS as concluded in Section 5.

7.1 Handling periodic mesh

To facilitate the query of topological information on the mesh, such as incident vertices or faces, we merge each pair of periodic vertices into a single vertex. The position of this vertex is taken from either of the two original vertices. This merging operation may result in elongated edges, which we exploit to identify whether an incident vertex belongs to another period (Figure 12). Specifically, when accessing the incident vertices of a given vertex, we check the difference vector between their positions. If any component of the vector exceeds 1 or falls below -1, we translate the incident vertex along that axis by $2k$ or $-2k$ until the difference lies within the range $[-1, 1]$ (Figure 12). These translated vertices are only used on the fly and are not stored back to the mesh data structure. With such operation, the mesh becomes locally equivalent to the periodic one. When updating vertex positions during the flow (Section 6.2.3), only a small translation vector is applied to each vertex, which does not interfere with the aforementioned operation. While long edges not caused by merging could potentially pose a problem, we avoid this by keeping the edge lengths less than 0.3 during the remeshing process (Section 18). Note that the remeshing algorithm involves only local operations, such as vertex translation, edge collapse (split), and edge flipping, this operation is not affected either.

7.2 Generation of periodic surface

To validate the conclusions in Section 5, we generate 15 types of TPMS (Figure 13 inset) using Surface Evolver [Brakke 1992], and sample 1000 non-TPMS surfaces for numerical experiments. All surfaces are rescaled to $Y = [-1, 1]^3$. The non-TPMS surfaces are sampled by perturbing the trigonometric approximations of Schwarz P, Schwarz D, IWP, and Gyroid, which are the level sets of the following functions:

$$\begin{aligned}
 \varphi_P(\mathbf{r}) &= \cos(2\pi x) + \cos(2\pi y) + \cos(2\pi z) \\
 \varphi_G(\mathbf{r}) &= \sin(2\pi x) \cos(2\pi y) + \sin(2\pi z) \cos(2\pi x) + \sin(2\pi y) \cos(2\pi z) \\
 \varphi_D(\mathbf{r}) &= \sin(2\pi x) \sin(2\pi y) \sin(2\pi z) + \sin(2\pi x) \cos(2\pi y) \cos(2\pi z) \\
 &\quad + \cos(2\pi x) \sin(2\pi y) \cos(2\pi z) + \cos(2\pi x) \cos(2\pi y) \sin(2\pi z) \\
 \varphi_{IWP}(\mathbf{r}) &= 2[\cos(2\pi x) \cos(2\pi y) + \cos(2\pi y) \cos(2\pi z) \\
 &\quad + \cos(2\pi z) \cos(2\pi x)] - [\cos(2 \cdot 2\pi x) + \cos(2 \cdot 2\pi y) + \cos(2 \cdot 2\pi z)].
 \end{aligned} \tag{32}$$

We perturb their level sets by adding an additional noise term: $\delta\varphi = \sum_i s_i b^i(\mathbf{x})$, where $b^i(\mathbf{x})$ denotes the basis functions; s_i are the coefficients randomly sampled from a uniform distribution over $[-\bar{s}, \bar{s}]$, with the parameter \bar{s} used to control the perturbation strength. The basis functions are drawn from the set $B_N := T_N \cup \{pq : p \in T_N, q \in T_N\}$, where $T_N = \{\sin(2\pi kx_i), \cos(2\pi kx_i)\}_{k=1, \dots, N}$. Here, integer N controls the degrees of freedom (DoF) in the perturbation. We observe that choosing $N \geq 2$ often produces overly noisy surfaces; therefore, we set $N = 1$ in our experiments. We evaluate the perturbed function $\tilde{\varphi} := \varphi + \delta\varphi$ on a $128 \times 128 \times 128$ grid evenly discretizing domain $[0, 1]^3$, where φ denotes any of the functions in (32). The level set surface is extracted from the grid values using the Marching Cube algorithm [Lorensen and Cline 1987] implemented in `libigl` [Jacobson et al. 2018]. We then improve the mesh quality using the incremental isotropic remeshing algorithm [Botsch et al. 2010]. We set the perturbation strength $\bar{s} = 0.1, 0.2, 0.3, 0.4, 0.5$, and for each setting, we sample the coefficients $\{s_i\}$

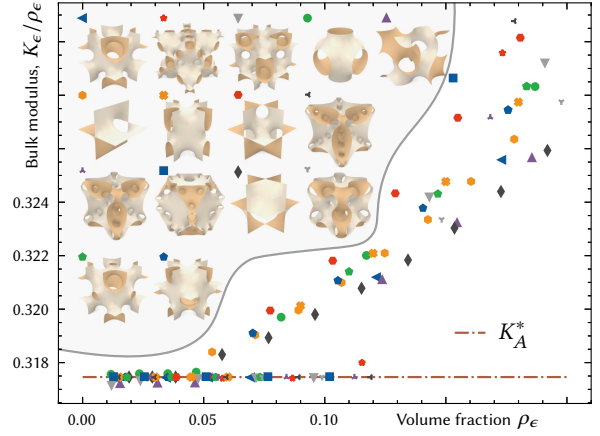


Fig. 13. Scatter plot of the the normalized bulk modulus (K_ϵ/ρ_ϵ) of 15 types of TPMS (inset) as the thickness approaches zero. The upper bound $K_A^* \approx 0.3174$ in our setting.

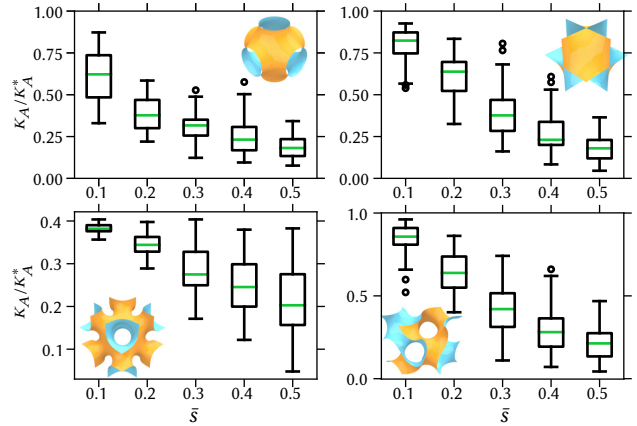


Fig. 14. The ABM of perturbed surfaces derived from Schwarz P, Schwarz D, IWP, and Gyroid. Each subplot corresponds to one TPMS type. The abscissa denotes the perturbation strength \bar{s} , with 50 surfaces sampled for each setting. Here, K_A^* denotes the upper bound in Theorem 5.

for 50 times, generating 50 perturbed surfaces. These surfaces are used to validate the ABM upper bound (Section 7.5) and as inputs to our optimization algorithm.

7.3 Simulation setup

We import the generated surfaces to ABAQUS for finite element simulation. Each triangular facet of the surface mesh is assigned a STRI3 shell element for mechanical simulation. The Young's modulus and Poisson's ratio are set to $Y = 1$ and $\nu = 0.3$, respectively. We use the Micromechanics plugin to enforce periodic boundary conditions and compute the effective elastic tensor.

7.4 Convergence test

According to the definition of asymptotic elastic tensor (6), it suffices to validate the following relation

$$C_A = \lim_{\epsilon \rightarrow 0} \frac{C_\epsilon}{\rho_\epsilon(\tilde{\omega})},$$

where C_A is defined in (7). To assess the convergence, we introduce the following relative error

$$\mathcal{E}^s := \frac{\|C_A^h - C_\epsilon/\rho_\epsilon\|_F}{\|C_A^h\|_F},$$

where C_A^h is given in (21), and C_ϵ is obtained from the simulations in ABAQUS. We generate the following level set surface for test

$$\varphi(\mathbf{r}) = 1.2 \cos(\pi x) + 0.9 \cos(\pi y) + 1.5 \cos(\pi z).$$

The surface mesh is extracted using the method in Section 7.2. We refine it using the remeshing algorithm in Section 18, setting the target edge length to $0.1 \times (4/5)^k$, where k denotes the refined times. After each refinement, the vertices are projected to the level set through a binary search along the gradient direction. We then evaluate C_A^h and the corresponding average circumradius of the mesh faces (considered as element size h). On the other hand, we import mesh to ABAQUS for simulation, with a decreasing shell thickness $2\epsilon = 0.1 \times (4/5)^k$. The error \mathcal{E}^s for each pair of h and 2ϵ is plotted in Figure 15. It shows that the error tends to zero when h and ϵ decrease simultaneously.

Next, we construct three revolution surfaces around the x -axis (Figure 16 inset), for which the ADS under strain \mathbf{e}^{11} can be solved semi-analytically (SM Section 5). Then we compare the ADS (E_A^h) obtained from our approach with the semi-analytical solution (E_A) under strain \mathbf{e}^{11} . We evaluate the relative error

$$\mathcal{E}^h := \frac{|E_A^h - E_A|}{|E_A|}$$

using a decreasing element size (h).

The experimental results (Figure 16) show a linear or even better convergence rate.

While we have no theoretical guarantee for the convergence of this discretization scheme, we argue that the variational problem (5) determining ADS is fundamentally difficult to discretize with guaranteed convergence. The reason is twofold. First, the function space is generally too large, possibly beyond the space of distributions, as noted in [Ciarlet and Lods 1996a; Meunier and Sanchez-Palencia

2006]. This leaves the linear form (RHS of (5)) in a very small dual space $(\tilde{V}_\#(\tilde{\omega}))'$, making it unclear whether the discretized form still defines a valid functional in this space, or whether the discretization can approximate the solutions that may not be regular functions. Second, the ADS could be extremely sensitive to the geometric perturbations in special cases, where an infinitesimally small error in the geometry could result in a significant change in the ADS (SM Section 6).

7.5 The optimality of TPMS

We validate the conclusions in Section 5. For the generated 15 types of TPMS (Section 7.2), we approximate C_A by C_ϵ/ρ_ϵ with a decreasing thickness, and use identity $K_A = \frac{1}{9}C_A : \mathbf{I} : \mathbf{I}$ to compute ABM. The approximated ABMs and their corresponding volume fractions are shown in Figure 13. The results indicate that the ABMs are very close to the upper bound, even when the volume fraction is relatively large ($< 20\%$).

On the other hand, the ABMs of non-TPMS surfaces are approximated in the same way with a fixed thickness of 0.004. The simulation results for the relative magnitudes K_A/K_A^* are shown in Figure 14. We observe that $K_A/K_A^* \leq 1$ for all these surfaces. Moreover, as the perturbation strength increases, this value tends to decrease as they are getting distinct from TPMS⁷. These numerical results conform to our theoretical prediction.

8 Validation of the optimization algorithm

8.1 Optimize ADS

Young's modulus. We maximize Young's modulus in different directions with a single input surface. The directional Young's modulus [Schumacher et al. 2018] is given by

$$Y_{\mathbf{z}}(C_A) = \left(\boldsymbol{\sigma}_{\mathbf{z}} : (C_A)^{-1} : \boldsymbol{\sigma}_{\mathbf{z}} \right)^{-1},$$

where $\boldsymbol{\sigma}_{\mathbf{z}} = \mathbf{z}\mathbf{z}^\top$ and \mathbf{z} denotes the direction in which Young's modulus is computed. We use AutoDiff module of the Eigen library [Guennebaud et al. 2010] to compute its derivative. The Young's modulus distributions of the surfaces before and after optimization are shown in Figure 17. A significant increase in stiffness is observed for various objective directions after optimization.

Shear modulus. Next, we maximize the stiffness under shear strains \mathbf{e}^{23} , \mathbf{e}^{13} , and \mathbf{e}^{12} with different input surfaces. Thanks to the surgery operation, the optimization removes the topological barriers and yields a better result (Figure 18). See also an application in Figure 19.

Bulk modulus. As Theorem 5 indicates, the upper bound of ABM is $K_A^* = \frac{4}{9}(\lambda_0 + \mu) \approx 0.3174$ under our experimental setting, and is achieved when the surface is a TPMS. Therefore, we conduct experiments with ABM as the objective to observe how the surfaces deform after optimization. The results are shown in Figure 20. Interestingly, the surfaces converge toward TPMS-like shapes with an increased ABM, consistent with our theoretical predictions.

⁷The ABMs of the perturbed IWP surfaces are exceptionally low, which may be attributed to either the poor accuracy of the trigonometric representation of IWP or the sensitive problem of the ADS, as discussed in Section 7.4.

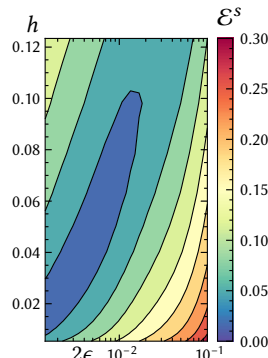


Fig. 15

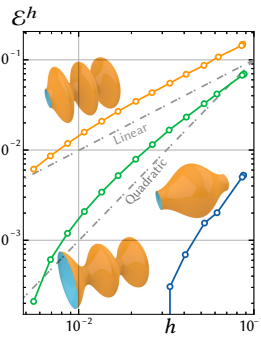


Fig. 16

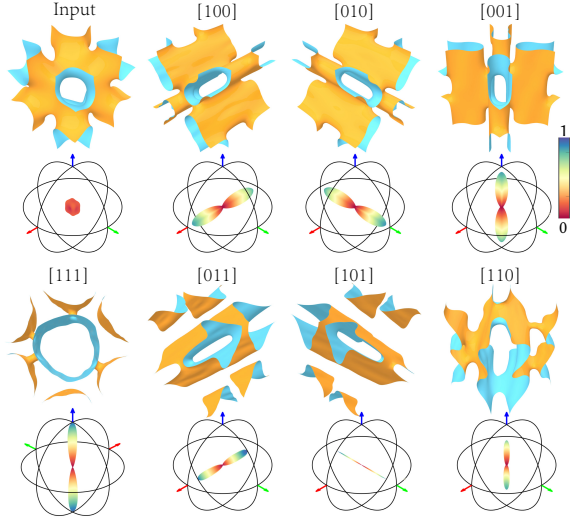


Fig. 17. Distribution of Young's modulus before and after optimization, visualized by VELAS [Ran et al. 2023]. The objective directions (z) of Young's modulus are noted above the surfaces.

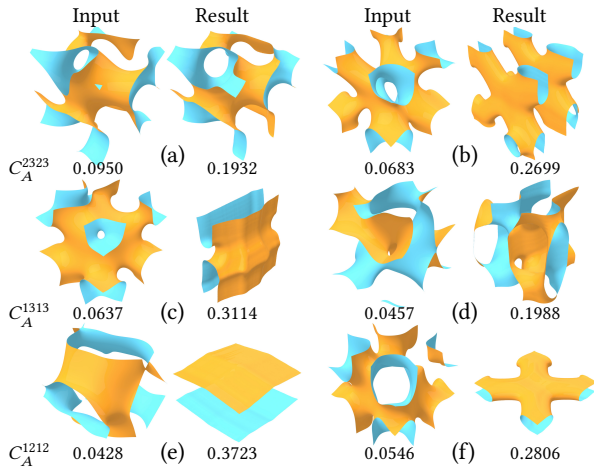


Fig. 18. Maximizing stiffness under three shear strains e^{23} (Top), e^{13} (Middle), and e^{12} (Bottom). The corresponding values of the objectives are noted below the surfaces.

Arbitrary strain. We can apply our approach to maximize the stiffness under arbitrary strains. Figure 21 shows the improvement in ADS under two representative strains. Optimizing ADS over a range of strains is also supported. For instance, we consider the average ADS under deviatoric strain $s = \text{diag}(1, -2, 1)$, integrated over all spatial orientations. The corresponding objective is:

$$f_s(C_A) = \int_{SO(3)} \varepsilon(\mathbf{R}) : C_A : \varepsilon(\mathbf{R}) d\mu(\mathbf{R})$$

where $\varepsilon(\mathbf{R}) = \mathbf{R}s\mathbf{R}^T$ denotes the rotated strain tensor under the orientation $\mathbf{R} \in SO(3)$, and $d\mu(\mathbf{R})$ is the Haar measure on $SO(3)$. The computation (SM Section 7) shows that this objective simplifies to

$$f_s(C_A) = \sum_i C_A^{iiii} + 3 \sum_{i \neq j} C_A^{ijij} - \sum_{i \neq j} C_A^{iijj}.$$

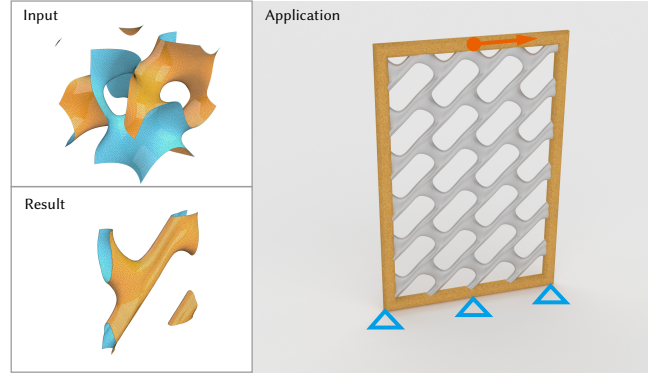


Fig. 19. Steel tube with optimized shear modulus is used to strengthen a frame. The red arrow denotes the load.

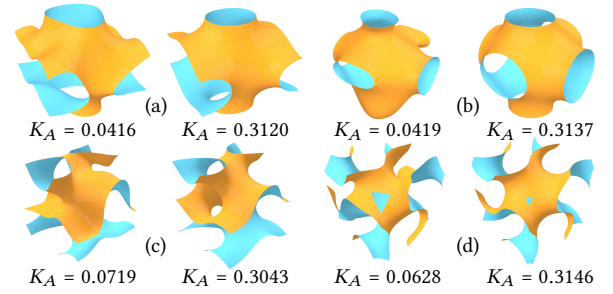


Fig. 20. Surfaces converge to TPMS-like shapes when optimizing ABM. The first and third columns show the input surfaces, and second and fourth columns show the optimized results.

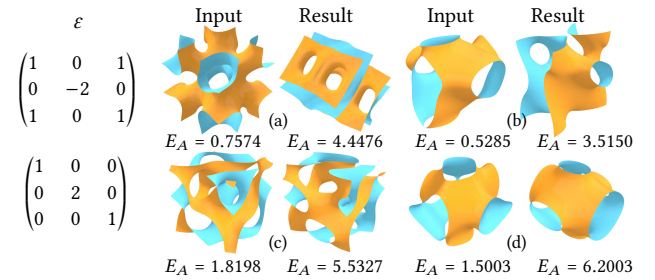


Fig. 21. Optimization of stiffness under specific strains (noted on the left side).

A demonstration is shown in Figure 22.

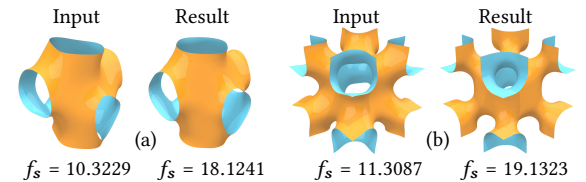


Fig. 22. Optimizing ADS under the deviatoric strain $s = \text{diag}(1, -2, 1)$ over all spatial orientations. Each result shows an increase in the objective value f_s after optimization.

Custom objective. Custom objective is also supported. For instance, we can add an isotropic penalty $f_{iso}^s(C_A)$ (Appendix E) to the objective when optimizing ABM, i.e., we employ the following objective

$$f(C_A) = \frac{1}{9} \mathbf{I} : C_A : \mathbf{I} - c f_{iso}^s(C_A),$$

where c is a constant penalty coefficient. A comparison across different values of c is shown in Figure 23.

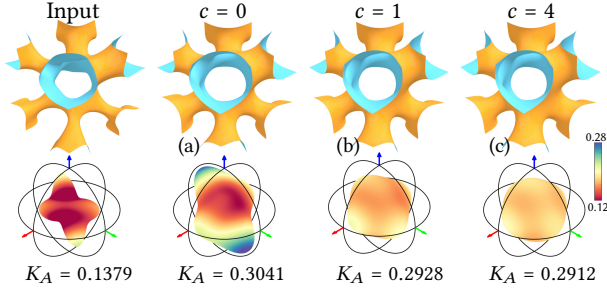


Fig. 23. Distribution of Young's modulus after optimization with different isotropic penalty coefficients (top), visualized by VELAS [Ran et al. 2023]. The corresponding ABM values are shown below.

We clarify that our method is not suitable for designing surfaces with a specified asymptotic elastic tensor or for minimizing stiffness under some strains. The reason is that when the objective encourages more compliant behavior—such as minimizing stiffness or targeting small ADS values—the surface tends to form wrinkles that help reduce stiffness. However, this often compromises the smoothness of the mesh, making our approximation inaccurate. See the example of designing metamaterials with a negative Poisson's ratio⁸ in Figure 24. The employed objective is elaborated in Appendix F.

REMARK 8. *Although it has been demonstrated that high-frequency surface details can enhance structural stability [Montes Maestre et al. 2023], such details may introduce manufacturing defects in metamaterials, as the physical size of the unit cell is typically small, making the intricate features difficult to reproduce accurately. Besides, they increase the risk of stress concentration. Therefore, despite this being a limitation of ADS, we believe that smoother surfaces are generally more desirable in practice.*

REMARK 9. *Additionally, we believe the shell lattices can still exhibit strong structural stability, such as buckling resistance, even with a fairly smooth middle surface and as thickness approaches zero, provided that the inextensional displacement space (i.e., $\ker \gamma$) degenerates to zero. This space contains the most likely buckling deformations, as they induce no membrane strain. A possible approach to enhancing structural stability based on this insight is left in the future work, as we will discuss in Section 9.*

8.2 Evolution of effective properties of shell lattice

To validate whether optimizing ADS of the middle surfaces improves the effective stiffness of the shell lattice, we conduct experiments maximizing K_A and C_A^{2323} . The evolution of the objectives during

⁸A negative Poisson's ratio is typically associated with a compliant material.

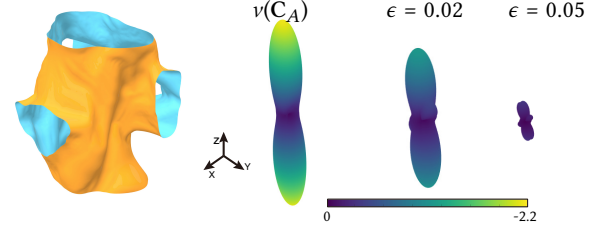


Fig. 24. Minimizing the Poisson's ratio in the z -direction. The wrinkles appear on the optimized surface (Left). The distribution of the negative Poisson's ratio is shown on the right, visualized by VELAS [Ran et al. 2023]. Although the Poisson's ratio $\nu(C_A)$ of the surface attains -2.2 (Right first), it decreases rapidly as the thickness increases (Right second and third).

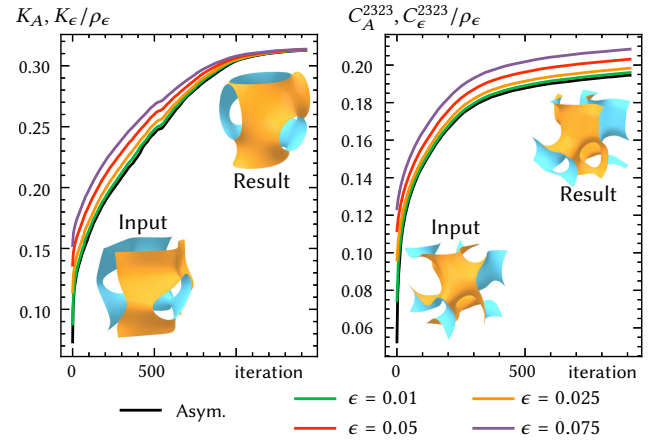


Fig. 25. The objective evolution of the derived shell lattices with different thickness (2ϵ) during the optimization, normalized by the volume fraction ($\rho\epsilon$). 'Asym.' represents the objective evaluated from C_A .

optimization, for both the asymptotic and effective stiffness of the derived shell lattices with varying thicknesses, is shown in Figure 25. The results demonstrate that the effective stiffness exhibits the same trend as the asymptotic stiffness during the optimization. Performance improvements for other optimized shell lattices in this work are summarized in Table 1.

8.3 Comparisons

A major distinction from traditional approaches based on shell elements is that our formulation and optimization of ADS focus exclusively on the geometry of the middle surface, independent of the shell's thickness. By definition, shell lattices optimized for higher ADS exhibit high, albeit not necessarily optimal, performance across a range of thicknesses with theoretical guarantees. This makes our approach particularly suitable for design scenarios where the thickness remains undetermined. In contrast, the optimization that uses shell elements with a specific thickness introduces uncertainty regarding stiffness when the thickness varies, thus multiple optimizations are necessary.

Another advantage lies in our discretization scheme. A typical Reissner-Mindlin plate element used in non-parametric design [Shimoda and Liu 2014] assigns five DoFs to each node, while our method

Table 1. Improvement of effective stiffness across different thicknesses (2ϵ). $H_{2\epsilon}^r$ denotes the relative increase of the objective $f(C_\epsilon/\rho_\epsilon)$, normalized by the corresponding increase in the objective $f(C_A)$ after optimization. For the surfaces in Figure 23, the increase is computed without the penalty term.

Surface	$H_{0.02}^r$	$H_{0.05}^r$	$H_{0.1}^r$	$H_{0.15}^r$	Surface	$H_{0.02}^r$	$H_{0.05}^r$	$H_{0.1}^r$	$H_{0.15}^r$
Fig. 17 [100]	97%	93%	90%	87%	Fig. 20 (a)	96%	87%	78%	71%
Fig. 17 [010]	96%	89%	82%	77%	Fig. 20 (b)	89%	78%	69%	61%
Fig. 17 [001]	93%	84%	77%	72%	Fig. 20 (c)	93%	84%	75%	70%
Fig. 17 [011]	96%	91%	88%	85%	Fig. 20 (d)	90%	76%	64%	56%
Fig. 17 [101]	97%	93%	89%	87%	Fig. 21 (a)	96%	89%	82%	78%
Fig. 17 [110]	98%	96%	94%	92%	Fig. 21 (b)	96%	89%	83%	80%
Fig. 17 [111]	97%	95%	93%	91%	Fig. 21 (c)	89%	77%	68%	63%
Fig. 18 (a)	86%	70%	58%	52%	Fig. 21 (d)	93%	87%	82%	77%
Fig. 18 (b)	89%	80%	73%	69%	Fig. 22 (a)	87%	67%	52%	43%
Fig. 18 (c)	95%	89%	85%	83%	Fig. 22 (b)	73%	55%	48%	41%
Fig. 18 (d)	92%	86%	80%	76%	Fig. 23 (a)	77%	57%	42%	34%
Fig. 18 (e)	99%	96%	93%	90%	Fig. 23 (b)	77%	58%	44%	36%
Fig. 18 (f)	97%	93%	89%	86%	Fig. 23 (c)	77%	58%	44%	36%
Fig. 19	90%	78%	70%	66%					

only assigns three DoFs. This reduces the size of the linear system to be solved in the analysis step, thus decreasing computational costs. A similar issue arises when resorting to subdivision surfaces [Bandara and Cirak 2018; Bandara et al. 2016; Cirak and Long 2010], where numerical integration is much more expensive. For parametric design methods [Bletzinger and Ramm 1993; Ma et al. 2022; Ramm et al. 1993] based on NURBS or Bézier patches, it becomes difficult to handle surfaces with complex topology, not only for the generation of the quadrilateral layout on a periodic surface, but also for addressing the continuity problem between patches and necking singularities that could appear during the optimization.

REMARK 10. *As thickness approaches zero, the higher-order infinitesimal bending energy in facet-based shell elements vanishes much more rapidly than the membrane strain energy, making the elements degenerate into plane (membrane) elements. This essentially reduces the necessary DoFs for evaluating strain energy. However, a simple plane element fails to capture surface deformation, as shown in Figure 5 middle. Therefore, our scheme (19) could be considered as an improved membrane element, retaining less DoFs than shell elements while capable of characterizing curved surfaces and their deformation.*

9 Conclusion

In this work, we introduce asymptotic directional stiffness (ADS) to quantify the influence of the middle surfaces to the stiffness of shell lattices. We establish the convergence theorem that provides its formulation. Based on this formulation, we derive an upper bound of ADS and establish the necessary and sufficient condition to achieve the bound. This condition is applied to justify the optimal bulk modulus of TPMS shell lattice metamaterials. To construct surfaces with higher ADS in a general case, we propose numerical methods for evaluating and optimizing the ADS of periodic surfaces. The simulation results validate our theoretical prediction and demonstrate the effectiveness of both the discretization and optimization algorithms.

Limitation and future work. Our optimization pipeline and implementation are not optimized for computational performance.

Acceleration techniques, such as Nesterov or Anderson acceleration [d’Aspremont et al. 2021], could be integrated into our algorithm. However, as the topology of the mesh changes during the optimization, such application is not straightforward. Additionally, more efficient solvers, such as geometric multigrid solvers [Briggs et al. 2000], could be used to solve the linear systems more efficiently.

The surgery operation is limited to simplifying the topology of the input surface. As a result, the final optimized geometry is dependent on the initial topology; for example, our method cannot generate a high-genus surface from a low-genus initial shape. We anticipate that other topological operations beyond surgery could be explored in future work. An alternative approach is using implicit representations for the surface, such as level set representation, which are more flexible to detect and handle topological variations.

Self-intersections have been observed in the experiments, which not only violates our assumption on the surface (embedding condition), but also introduces manufacturing problems, such as the creation of closed chambers. In future work, we plan to incorporate repulsive energy terms as proposed in [Sassen et al. 2024; Yu et al. 2021a] to solve the problem. Other manufacturing constraints like overhang angle constraint should also be taken into account.

As indicated by the formulation of ADS, it does not capture the bending stiffness of shell lattices. Pure bending deformations are essentially located in the inextensional displacement space ($\ker \gamma$). Shell structures are typically much less resistant to such deformations, as bending energy is of higher-order infinitesimal compared to membrane energy, and bending deformation induces significant stress near the boundary surfaces of shell. To identify these unstable deformation modes, one can solve the following eigenvalue problem

$$\min_{\mathbf{u} \in \mathbf{H}^1(\tilde{\omega}) \cap \text{Rig}^\perp} \int_{\tilde{\omega}} \gamma(\mathbf{u}) : \mathbf{A}_{\tilde{\omega}} : \gamma(\mathbf{u}) \quad \text{s.t.} \quad \|\mathbf{u}\|_{L^2(\tilde{\omega})}^2 = 1$$

based on our discrete scheme for $\gamma(\mathbf{u})$. Consequently, maximizing this minimum eigenvalue provides a possible strategy to reduce bending effects, and enhance buckling strength.

Acknowledgments

We thank the anonymous reviewers for their constructive feedback. We are also grateful to Xiaoming Fu, Xiaoya Zhai, and Qing Fang for insightful discussions on potential applications of the theory, and to Tian Wu for reviewing the proof in an early draft. This work is supported by the National Key R&D Program of China (2022YFB3303400) and the National Natural Science Foundation of China (62025207).

References

- Oraib Al-Ketan, Mohamed Ali, Mohamad Khalil, Reza Rowshan, Kamran A. Khan, and Rashid K. Abu Al-Rub. 2020. Forced Convection Computational Fluid Dynamics Analysis of Architected and Three-Dimensional Printable Heat Sinks Based on Triply Periodic Minimal Surfaces. *Journal of Thermal Science and Engineering Applications* 13, 2 (07 2020), 021010.
- Grégoire Allaire. 2002. *Shape Optimization by the Homogenization Method* (1 ed.). Springer New York, NY, XVI, 458 pages.
- Kosala Bandara and Fehmi Cirak. 2018. Isogeometric shape optimisation of shell structures using multiresolution subdivision surfaces. *Computer-Aided Design* 95 (2018), 62–71.
- Kosala Bandara, Thomas Rübberg, and Fehmi Cirak. 2016. Shape optimisation with multiresolution subdivision surfaces and immersed finite elements. *Computer Methods in Applied Mechanics and Engineering* 300 (2016), 510–539.

- M. Bernadou, P. G. Ciarlet, and B. Miara. 1994. Existence theorems for two-dimensional linear shell theories. *Journal of Elasticity* 34, 2 (01 Feb 1994), 111–138.
- Kai-Uwe Bletzinger, Matthias Firl, Johannes Linhard, and Roland Wüchner. 2010. Optimal shapes of mechanically motivated surfaces. *Computer Methods in Applied Mechanics and Engineering* 199, 5 (2010), 324–333. Computational Geometry and Analysis.
- K-U Bletzinger and E Ramm. 1993. Form finding of shells by structural optimization. *Engineering with Computers* 9, 1 (March 1993), 27–35.
- Kai-Uwe Bletzinger, Roland Wüchner, Fernað Daoud, and Natalia Camprubi. 2005. Computational methods for form finding and optimization of shells and membranes. *Computer Methods in Applied Mechanics and Engineering* 194, 30 (2005), 3438–3452. Structural and Design Optimization.
- Colin Bonatti and Dirk Mohr. 2019. Smooth-shell metamaterials of cubic symmetry: Anisotropic elasticity, yield strength and specific energy absorption. *Acta Materialia* 164 (2019), 301–321.
- Mario Botsch and Leif Kobbelt. 2004. An intuitive framework for real-time freeform modeling. In *ACM SIGGRAPH 2004 Papers* (Los Angeles, California) (SIGGRAPH '04). Association for Computing Machinery, New York, NY, USA, 630–634.
- Mario Botsch, Leif Kobbelt, Mark Pauly, Pierre Alliez, and Bruno Levy. 2010. *Polygon Mesh Processing*. A K Peters/CRC Press.
- Kenneth A. Brakke. 1992. The surface evolver. *Experimental Mathematics* 1, 2 (1992), 141–165.
- William L. Briggs, Van Emden Henson, and Steve F. McCormick. 2000. *A Multigrid Tutorial, Second Edition* (second ed.). Society for Industrial and Applied Mathematics.
- Shouyu Cai, Hualin Zhang, and Weihong Zhang. 2023. An integrated design approach for simultaneous shape and topology optimization of shell structures. *Computer Methods in Applied Mechanics and Engineering* 415 (2023), 116218.
- Xueyan Chen, Qingxiang Ji, Jianzheng Wei, Huifeng Tan, Jianxin Yu, Pengfei Zhang, Vincent Laude, and Muamer Kadic. 2020. Light-weight shell-lattice metamaterials for mechanical shock absorption. *International Journal of Mechanical Sciences* 169 (2020), 105288.
- Zeyao Chen, Yi Min Xie, Xian Wu, Zhe Wang, Qing Li, and Shiwei Zhou. 2019. On hybrid cellular materials based on triply periodic minimal surfaces with extreme mechanical properties. *Materials & Design* 183 (2019), 108109.
- Philippe G Ciarlet and Véronique Lods. 1996a. Asymptotic analysis of linearly elastic shells: ‘Generalized membrane shells’. *Journal of Elasticity* 43, 2 (May 1996), 147–188.
- Philippe G. Ciarlet and Véronique Lods. 1996b. Asymptotic analysis of linearly elastic shells. I. Justification of membrane shell equations. *Archive for Rational Mechanics and Analysis* 136, 2 (01 Dec 1996), 119–161.
- Philippe G. Ciarlet, Véronique Lods, and Bernadette Miara. 1996. Asymptotic analysis of linearly elastic shells. II. Justification of flexural shell equations. *Archive for Rational Mechanics and Analysis* 136, 2 (01 Dec 1996), 163–190.
- Fehmi Cirak and Quan Long. 2010. *Advances in Subdivision Finite Elements for Thin Shells*. Springer Vienna, Vienna, 205–227.
- Biwei Deng and Gary J. Cheng. 2021. Soap film inspired mechanical metamaterials approaching theoretical bound of stiffness across full density range. *Materials Horizons* 8, 3 (2021), 987–996.
- Alexandre d’Aspremont, Damien Scieur, and Adrien Taylor. 2021. Acceleration Methods. *Foundations and Trends® in Optimization* 5, 1–2 (2021), 1–245.
- Jiawei Feng, Jianzhong Fu, Xinhua Yao, and Yong He. 2022. Triply periodic minimal surface (TPMS) porous structures: from multi-scale design, precise additive manufacturing to multidisciplinary applications. *International Journal of Extreme Manufacturing* 4, 2 (mar 2022), 022001.
- Jiawei Feng, Bo Liu, Zhiwei Lin, and Jianzhong Fu. 2021. Isotropic porous structure design methods based on triply periodic minimal surfaces. *Materials & Design* 210 (2021), 110050.
- Eitan Grinspun, Anil N. Hirani, Mathieu Desbrun, and Peter Schröder. 2003. Discrete Shells. In *Symposium on Computer Animation*, D. Breen and M. Lin (Eds.). The Eurographics Association.
- Gaël Guennebaud, Benoît Jacob, et al. 2010. Eigen v3. <http://eigen.tuxfamily.org>.
- Z. Hashin and S. Shtrikman. 1963. A variational approach to the theory of the elastic behaviour of multiphase materials. *Journal of the Mechanics and Physics of Solids* 11, 2 (1963), 127–140.
- Emmanuel Hebey. 1996. *Sobolev Spaces on Riemannian Manifolds* (1 ed.). Springer Berlin, Heidelberg. XII, 120 pages. Published: 02 October 1996.
- Michael Hemmer. 2024. Algebraic Foundations. In *CGAL User and Reference Manual* (5.6.2 ed.). CGAL Editorial Board.
- T Hirschler, R Bouclier, A Duval, T Elguedj, and J Morlier. 2019. Isogeometric sizing and shape optimization of thin structures with a solid-shell approach. *Structural and Multidisciplinary Optimization* 59, 3 (March 2019), 767–785.
- Jiangbei Hu, Shengfa Wang, Baojun Li, Fengqi Li, Zhongxuan Luo, and Ligang Liu. 2022. Efficient Representation and Optimization for TPMS-Based Porous Structures. *IEEE Transactions on Visualization and Computer Graphics* 28, 7 (2022), 2615–2627.
- T.J.R. Hughes, J.A. Cottrell, and Y. Bazilevs. 2005. Isogeometric analysis: CAD, finite elements, NURBS, exact geometry and mesh refinement. *Computer Methods in Applied Mechanics and Engineering* 194, 39 (2005), 4135–4195.
- Alec Jacobson, Daniele Panozzo, et al. 2018. libigl: A simple C++ geometry processing library. <https://libigl.github.io/>.
- Xudong Jiang, Weisheng Zhang, Chang Liu, Zongliang Du, and Xu Guo. 2023. An explicit approach for simultaneous shape and topology optimization of shell structures. *Applied Mathematical Modelling* 113 (2023), 613–639.
- Pilseong Kang and Sung-Kie Youn. 2016. Isogeometric shape optimization of trimmed shell structures. *Structural and Multidisciplinary Optimization* 53, 4 (April 2016), 825–845.
- Inderjot Kaur and Prashant Singh. 2021. Flow and thermal transport characteristics of Triply-Periodic Minimal Surface (TPMS)-based gyroid and Schwarz-P cellular materials. *Numerical Heat Transfer, Part A: Applications* 79, 8 (2021), 553–569.
- J. Kiendl, R. Schmidt, R. Wüchner, and K.-U. Bletzinger. 2014. Isogeometric shape optimization of shells using semi-analytical sensitivity analysis and sensitivity weighting. *Computer Methods in Applied Mechanics and Engineering* 274 (2014), 148–167.
- G. Kirchhoff. 1850. Über das Gleichgewicht und die Bewegung einer elastischen Scheibe. *Journal für die Reine und Angewandte Mathematik* 1850, 40 (1850), 51–88. Cited by: 1053; All Open Access, Green Open Access.
- Hiroki Kobayashi, Katsuya Nomura, Yuqing Zhou, Masato Tanaka, Atsushi Kawamoto, and Tsuyoshi Nomura. 2024. Shell topology optimization based on level set method. *Structural and Multidisciplinary Optimization* 67, 8 (Aug. 2024), 151.
- Balázs Kovács. 2024. Numerical Surgery for Mean Curvature Flow of Surfaces. *SIAM Journal on Scientific Computing* 46, 2 (2024), A645–A669.
- Yang Liu, Yongzhen Wang, Hongyuan Ren, Zhiqiang Meng, Xueqian Chen, Zuyu Li, Liwei Wang, Wei Chen, Yifan Wang, and Jianbin Du. 2024. Ultrastiff metamaterials generated through a multilayer strategy and topology optimization. *Nature Communications* 15, 1 (April 2024), 2984.
- William E. Lorensen and Harvey E. Cline. 1987. Marching cubes: A high resolution 3D surface construction algorithm. In *Proceedings of the 14th Annual Conference on Computer Graphics and Interactive Techniques (SIGGRAPH '87)*. Association for Computing Machinery, New York, NY, USA, 163–169.
- Augustus Edward Hough Love. 1888. The small free vibrations and deformation of a thin elastic shell. *Philosophical Transactions of the Royal Society of London.(A.)* 179 (1888), 491–546.
- Long Ma, Ying He, Qian Sun, Yuanfeng Zhou, Caiming Zhang, and Wenping Wang. 2019. Constructing 3D Self-Supporting Surfaces with Isotropic Stress Using 4D Minimal Hypersurfaces of Revolution. *ACM Trans. Graph.* 38, 5, Article 144 (Oct. 2019), 13 pages.
- Qingping Ma, Lei Zhang, Junhao Ding, Shuo Qu, Jin Fu, Mingdong Zhou, Ming Wang Fu, Xu Song, and Michael Yu Wang. 2021. Elastically-isotropic open-cell minimal surface shell lattices with superior stiffness via variable thickness design. *Additive Manufacturing* 47 (2021), 102293.
- Qingping Ma, Lei Zhang, and Michael Yu Wang. 2022. Elastically isotropic open-cell uniform thickness shell lattices with optimized elastic moduli via shape optimization. *Materials & Design* 215 (2022), 110426.
- Liane Makatura, Bohan Wang, Yi-Lu Chen, Bolei Deng, Chris Wojtan, Bernd Bickel, and Wojciech Matusik. 2023. Procedural Metamaterials: A Unified Procedural Graph for Metamaterial Design. *ACM Trans. Graph.* 42, 5, Article 168 (jul 2023), 19 pages.
- Francesco Marmo and Nicolò Vaiana. 2021. *Form Finding of Shell Structures by Using Membrane Theory*. Springer International Publishing, Cham, 213–237.
- Jonás Martínez, Jérémie Dumas, and Sylvain Lefebvre. 2016. Procedural voronoi foams for additive manufacturing. *ACM Trans. Graph.* 35, 4, Article 44 (July 2016), 12 pages.
- Jonás Martínez, Samuel Hornus, Haichuan Song, and Sylvain Lefebvre. 2018. Polyhedral voronoi diagrams for additive manufacturing. *ACM Trans. Graph.* 37, 4, Article 129 (July 2018), 15 pages.
- Jonás Martínez, Mélina Skouras, Christian Schumacher, Samuel Hornus, Sylvain Lefebvre, and Bernhard Thomaszewski. 2019. Star-shaped metrics for mechanical metamaterial design. *ACM Trans. Graph.* 38, 4, Article 82 (July 2019), 13 pages.
- Jonás Martínez, Haichuan Song, Jérémie Dumas, and Sylvain Lefebvre. 2017. Orthotropic k-nearest foams for additive manufacturing. *ACM Trans. Graph.* 36, 4, Article 121 (July 2017), 12 pages.
- N. Meunier and E. Sanchez-Palencia. 2006. SENSITIVE VERSUS CLASSICAL SINGULAR PERTURBATION PROBLEM VIA FOURIER TRANSFORM. *Mathematical Models and Methods in Applied Sciences* 16, 11 (2006), 1783–1816.
- Masaaki Miki and Toby Mitchell. 2022. Interactive Exploration of Tension-Compression Mixed Shells. *ACM Trans. Graph.* 41, 6, Article 263 (Nov. 2022), 14 pages.
- Masaaki Miki and Toby Mitchell. 2024. Alignment conditions for NURBS-based design of mixed tension-compression grid shells. *ACM Trans. Graph.* 43, 4, Article 81 (July 2024), 19 pages.
- Graeme W. Milton. 2002. *The Theory of Composites*. Cambridge University Press.
- R D Mindlin. 1951. Influence of rotatory inertia and shear on flexural motions of isotropic, elastic plates. *J. Appl. Mech.* 18, 1 (March 1951), 31–38.
- Juan Sebastian Montes Maestre, Yinwei Du, Ronan Hinchet, Stelian Coros, and Bernhard Thomaszewski. 2023. Differentiable Stripe Patterns for Inverse Design of Structured Surfaces. *ACM Trans. Graph.* 42, 4, Article 102 (July 2023), 14 pages.

- Rahul Narain, Tobias Pfaff, and James F. O'Brien. 2013. Folding and crumpling adaptive sheets. 32, 4, Article 51 (July 2013), 8 pages.
- Julian Panetta, Abtin Rahimian, and Denis Zorin. 2017. Worst-case stress relief for microstructures. *ACM Trans. Graph.* 36, 4, Article 122 (jul 2017), 16 pages.
- Julian Panetta, Qingnan Zhou, Luigi Malomo, Nico Pietroni, Paolo Cignoni, and Denis Zorin. 2015. Elastic textures for additive fabrication. *ACM Trans. Graph.* 34, 4, Article 135 (jul 2015), 12 pages.
- Zahid Ahmed Qureshi, Emad Elnajjar, Oraib Al-Ketan, Rashid Abu Al-Rub, and Salah Burhan Al-Omari. 2021. Heat transfer performance of a finned metal foam-phase change material (FMF-PCM) system incorporating triply periodic minimal surfaces (TPMS). *International Journal of Heat and Mass Transfer* 170 (2021), 121001.
- Ekkehard Ramm, Kai-Uwe Bletzinger, and Reiner Reitinger. 1993. Shape optimization of shell structures. *Revue Européenne des Éléments Finis* 2, 3 (1993), 377–398.
- Zheng Ran, Chunming Zou, Zunjie Wei, and Hongwei Wang. 2023. VELAS: An open-source toolbox for visualization and analysis of elastic anisotropy. *Computer Physics Communications* 283 (2023), 108540.
- J N Reddy. 2006. *Theory and analysis of elastic plates and shells, second edition* (2 ed.). CRC Press, Boca Raton, FL.
- S. Rusinkiewicz. 2004. Estimating curvatures and their derivatives on triangle meshes. In *Proceedings. 2nd International Symposium on 3D Data Processing, Visualization and Transmission, 2004. 3DPVT 2004.* 486–493.
- Josua Sassen, Henrik Schumacher, Martin Rumpf, and Keenan Crane. 2024. Repulsive Shells. *ACM Trans. Graph.* 43, 4 (2024).
- Christian Schumacher, Bernd Bickel, Jan Rys, Steve Marschner, Chiara Daraio, and Markus Gross. 2015. Microstructures to control elasticity in 3D printing. *ACM Trans. Graph.* 34, 4, Article 136 (July 2015), 13 pages.
- Christian Schumacher, Steve Marschner, Markus Gross, and Bernhard Thomaszewski. 2018. Mechanical characterization of structured sheet materials. *ACM Trans. Graph.* 37, 4, Article 148 (July 2018), 15 pages.
- Masatoshi Shimoda and Yang Liu. 2014. A non-parametric free-form optimization method for shell structures. *Structural and Multidisciplinary Optimization* 50, 3 (Sept. 2014), 409–423.
- S. Torquato and A. Donev. 2004. Minimal surfaces and multifunctionality. *Proceedings of the Royal Society of London. Series A: Mathematical, Physical and Engineering Sciences* 460, 2047 (2004), 1849–1856.
- Davi Colli Tozoni, Jérémie Dumas, Zhongshi Jiang, Julian Panetta, Daniele Panozzo, and Denis Zorin. 2020. A low-parametric rhombic microstructure family for irregular lattices. *ACM Trans. Graph.* 39, 4, Article 101 (Aug. 2020), 20 pages.
- Woldemar Voigt. 1910. *Lehrbuch der kristallphysik:(mit ausschluss der kristalloptik)*. Vol. 34. BG Teubner.
- Shengfa Wang, Yu Jiang, Jiangbei Hu, Xin Fan, Zhongxuan Luo, Yongjin Liu, and Ligang Liu. 2022a. Efficient Representation and Optimization of TPMS-Based Porous Structures for 3D Heat Dissipation. *Computer-Aided Design* 142 (2022), 103123.
- Yongzhen Wang, Qinglei Zeng, Jizhen Wang, Ying Li, and Daining Fang. 2022b. Inverse design of shell-based mechanical metamaterial with customized loading curves based on machine learning and genetic algorithm. *Computer Methods in Applied Mechanics and Engineering* 401 (2022), 115571.
- Yujia Wang, Xuan Zhang, Zihe Li, Huajian Gao, and Xiaoyan Li. 2022c. Achieving the theoretical limit of strength in shell-based carbon nanolattices. *Proceedings of the National Academy of Sciences* 119, 34 (2022), e2119536119.
- Hong Xiao and Zydrunas Gimbutas. 2010. A numerical algorithm for the construction of efficient quadrature rules in two and higher dimensions. *Computers & Mathematics with Applications* 59, 2 (2010), 663–676.
- Yu Xing, Xiaoxuan Wang, Lin Lu, Andrei Sharf, Daniel Cohen-Or, and Changhe Tu. 2024. Shell stand: Stable thin shell models for 3D fabrication. *Computational Visual Media* 10, 4 (Aug. 2024), 643–657.
- Wenpeng Xu, Peng Zhang, Menglin Yu, Li Yang, Weiming Wang, and Ligang Liu. 2024. Topology Optimization Via Spatially-Varying TPMS. *IEEE Transactions on Visualization and Computer Graphics* 30, 8 (2024), 4570–4587.
- Xin Yan, Cong Rao, Lin Lu, Andrei Sharf, Haisen Zhao, and Baoquan Chen. 2020. Strong 3D Printing by TPMS Injection. *IEEE Transactions on Visualization and Computer Graphics* 26, 10 (2020), 3037–3050.
- Chris Yu, Caleb Brakensiek, Henrik Schumacher, and Keenan Crane. 2021a. Repulsive Surfaces. *ACM Trans. Graph.* 40, 6 (2021).
- Chris Yu, Henrik Schumacher, and Keenan Crane. 2021b. Repulsive Curves. *ACM Trans. Graph.* 40, 2 (2021).
- C. Zener. 1948. *Elasticity and Anelasticity of Metals*. University of Chicago Press.
- Weisheng Zhang, Shan Jiang, Chang Liu, Dingding Li, Pilsong Kang, Sung-Kie Youn, and Xu Guo. 2020. Stress-related topology optimization of shell structures using IGA/TSA-based Moving Morphable Void (MMV) approach. *Computer Methods in Applied Mechanics and Engineering* 366 (2020), 113036.

A Derivation of E_M

It suffices to derive the following equation

$$E_M(\tilde{\omega}; \varepsilon) = \varepsilon : \bar{\mathbb{P}} : \varepsilon = \int_{\tilde{\omega}} e_{\tilde{\omega}} : \mathbf{A}_{\tilde{\omega}} : e_{\tilde{\omega}}. \quad (33)$$

The strain $e_{\tilde{\omega}}$ can be written in matrix form as:

$$e_{\tilde{\omega}} = P\varepsilon P^T,$$

where $P = \mathbf{I} - \mathbf{nn}^T$ is the projection matrix. Then the integrand in (33), denoted as $f_M(\tilde{\omega}; \varepsilon)$ for brevity, becomes

$$\begin{aligned} f_M(\tilde{\omega}; \varepsilon) &= \lambda_0 P^{ik} P^{il} \varepsilon_{kl} P^{jm} P^{jn} \varepsilon_{mn} + 2\mu P^{ik} P^{jl} \varepsilon_{kl} P^{im} P^{jn} \varepsilon_{mn} \\ &= \varepsilon : \mathbb{P} : \varepsilon, \end{aligned}$$

where

$$\mathbb{P} := (\lambda_0 P^{ik} P^{il} P^{jm} P^{jn} + 2\mu P^{ik} P^{jl} P^{im} P^{jn}) \mathbf{e}_k \otimes \mathbf{e}_l \otimes \mathbf{e}_m \otimes \mathbf{e}_n.$$

Note that we are using the orthogonal basis, thus we sum over the duplicated indices, regardless of whether they are superscripts or subscripts. Given that P is a projection matrix, we have $P^T P = P$, or $P^{ik} P^{jl} = P^{kl}$ in component form. Therefore, \mathbb{P} is simplified as

$$[\mathbb{P}]^{ijkl} = \lambda_0 P^{ij} P^{kl} + \mu (P^{il} P^{jk} + P^{ik} P^{jl}).$$

Since ε is a constant tensor, we have

$$E_M(\tilde{\omega}; \varepsilon) = \frac{1}{|\tilde{\omega}|} \int_{\tilde{\omega}} \varepsilon : \mathbb{P} : \varepsilon = \varepsilon : \bar{\mathbb{P}} : \varepsilon,$$

where $\bar{\mathbb{P}} := \frac{1}{|\tilde{\omega}|} \int_{\tilde{\omega}} \mathbb{P}$ denotes the average of \mathbb{P} over $\tilde{\omega}$.

B Proof of Theorem 4

PROOF. The sum of eigenvalues of \mathbb{P} is

$$\sum_{i=1}^6 \lambda_i(\mathbb{P}) = \text{tr } \mathbb{P} = \mathbb{P} :: \mathbb{I}, \quad (34)$$

where \mathbb{I} is the fourth-order identity tensor:

$$\mathbb{I} = \delta_{ik} \delta_{jl} \mathbf{e}^i \otimes \mathbf{e}^j \otimes \mathbf{e}^k \otimes \mathbf{e}^l.$$

By computation, we have

$$\mathbb{P} :: \mathbb{I} = \lambda_0 P_{kl} P_{kl} + \mu (P_{kl} P_{kl} + P_{kk} P_{ll}).$$

Notice that

$$\begin{aligned} P_{kl} P_{kl} &= \text{tr } P P^T = \text{tr } P = 2 \\ P_{kk} P_{ll} &= (\text{tr } P)^2 = 4, \end{aligned} \quad (35)$$

where the last equalities of both equations hold because $\text{tr } P = \text{tr } (\mathbf{I} - \mathbf{nn}^T) = 2$. Hence, we get

$$\mathbb{P} :: \mathbb{I} = 2\lambda_0 + 6\mu. \quad (36)$$

Then we have

$$\sum_{i=1}^6 E_M(\tilde{\omega}; \varepsilon_i) = \frac{1}{|\tilde{\omega}|} \int_{\tilde{\omega}} \sum_i \varepsilon_i : \mathbb{P} : \varepsilon_i = \frac{1}{|\tilde{\omega}|} \int_{\tilde{\omega}} \sum_{i=1}^6 \lambda_i(\mathbb{P}) = 2\lambda_0 + 6\mu,$$

where we have utilized (34) and (36). \square

C Assemble the stiffness matrix and load vector

We first select a 2D orthonormal frame

$$P_f = (\mathbf{a}_1, \mathbf{a}_2)^\top \quad (37)$$

on each face as the coordinate basis to facilitate computation. The strain and stress tensor are stored in the Voigt representation [Voigt 1910] under this basis:

$$[e_f] = (e_f^{11}, e_f^{22}, 2e_f^{12})^\top.$$

The second fundamental form \mathbf{b}_f is approximated as the solution of the following equations for each edge vector \mathbf{l}_{ij} of the face f :

$$\mathbf{l}_{ij}^\top \mathbf{b}_f \mathbf{l}_{ij} = -(\mathbf{n}_i - \mathbf{n}_j) \cdot \mathbf{l}_{ij}.$$

Once \mathbf{b}_f is solved, the membrane strain is represented by

$$[y(\mathbf{u})] = (B_t - B_n)\mathbf{u}_f,$$

where $\mathbf{u}_f = (\mathbf{u}_1; \mathbf{u}_2; \mathbf{u}_3) \in \mathbb{R}^9$ stacks the three vertex displacement vectors, and B_t is the strain-displacement matrix mapping \mathbf{u}_f to the Voigt representation of $\text{Sym}[\nabla \mathbf{u}_t]$ with \mathbf{u}_t given by

$$\mathbf{u}_t = \sum_i \phi_i P_f R_i^f \mathbf{u}_i.$$

The matrix B_n has the following form

$$B_n = [\mathbf{b}_f](\phi_1 \mathbf{n}_1^\top, \phi_2 \mathbf{n}_2^\top, \phi_3 \mathbf{n}_3^\top),$$

where $[\mathbf{b}_f] = (b_f^{11}, b_f^{22}, 2b_f^{12})^\top$ and ϕ_i, \mathbf{n}_i denote the linear interpolation function (i.e., barycentric coordinate) and vertex normal, respectively. Then the element stiffness matrix for each face is

$$\mathbf{K}_f = \int_f [y(\mathbf{u})]^\top D [y(\mathbf{u})], \quad (38)$$

where D is the membrane elastic matrix given by

$$D = \begin{pmatrix} \lambda_0 + 2\mu & \lambda_0 & 0 \\ \lambda_0 & \lambda_0 + 2\mu & 0 \\ 0 & 0 & \mu \end{pmatrix}.$$

We use three point quadrature [Xiao and Gimbutas 2010] on triangles to evaluate this integral. The load vector on each face is discretized as

$$\mathbf{f}_f = - \int_f [y(\mathbf{u})]^\top D [P_f \varepsilon P_f^\top]. \quad (39)$$

Here, $[P_f \varepsilon P_f^\top]$ denotes the Voigt representation of the projected strain $P_f \varepsilon P_f^\top$. This integral is evaluated using single point quadrature. The element stiffness matrices in (38) and the load vectors in (39) are then assembled into the global stiffness matrix \mathbf{K}^h and load vector \mathbf{f}^h .

D Discretization of sensitivity

We discretize the normal velocity on the mesh as a linear interpolation from the normal velocity on vertex, given by

$$v_n^h := \sum_{i \in \mathcal{V}} v_n^i \phi_i,$$

where v_n^i is the normal velocity on i -th vertex. ϕ_i is the linear interpolation function.

Sensitivity of Area. The discretization of (23) is given by

$$\dot{A} \approx - \sum_{f \in \mathcal{F}} \int_f v_n^h \text{tr} \mathbf{b}_f = - \sum_{f \in \mathcal{F}} \sum_{i \in N(f)} v_n^i \int_f \phi_i \text{tr} \mathbf{b}_f,$$

where $N(f)$ denotes the vertices of face f . We use single point quadrature on each face to evaluate the integral.

Sensitivity of ADS. The time derivative \dot{I}_a^s is discretized as follows

$$\dot{I}_a^s \approx \sum_{f \in \mathcal{F}} \sum_{i \in N(f)} v_n^i \int_f 2\phi_i \left[B^h(\mathbf{u}^h, \mathbf{u}^h) - \frac{\text{tr} \mathbf{b}_f}{2} A^h(\mathbf{u}^h, \mathbf{u}^h) \right] + 2C_i^h(\mathbf{u}^h, \mathbf{u}^h).$$

Here, the symbols are computed as

$$\begin{aligned} A^h(\mathbf{u}^h, \mathbf{v}^h) &= e_f(\mathbf{u}^h) : \mathbf{A}_{\tilde{\omega}} : e_f(\mathbf{v}^h) \\ B^h(\mathbf{u}^h, \mathbf{v}^h) &= e_f(\mathbf{u}^h) : \mathbf{B}_{\tilde{\omega}} : e_f(\mathbf{v}^h) \\ C_i^h(\mathbf{u}^h, \mathbf{v}^h) &= e_f(\mathbf{u}^h) : \mathbf{A}_{\tilde{\omega}} : \zeta_i^h(\mathbf{v}^h), \end{aligned} \quad (40)$$

where the strain $e_f(\mathbf{u}^h)$ is given by

$$e_f(\mathbf{u}^h) = \text{Sym}[\mathbf{u}_t^h] - \mathbf{u}_3^h \mathbf{b}_f + P_f \varepsilon P_f^\top,$$

and P_f denotes the projection given in (37). The term $\zeta_i^h(\mathbf{u}^h)$ is defined as

$$\begin{aligned} \zeta_i^h(\mathbf{u}^h) &= \mathbf{b}_f \mathbf{u}_t^h (\nabla \phi_i)^\top - \phi_i \mathbf{b}_f \nabla \mathbf{u}_t^h + \nabla \mathbf{u}_3^h (\nabla \phi_i)^\top + \mathbf{u}_3^h \phi_i \mathbf{c}_f \\ &\quad + 2P_f \varepsilon \mathbf{n}_f (\nabla \phi_i)^\top, \end{aligned}$$

where \mathbf{n}_f denotes the normal vector of face f and $\mathbf{c}_f = \mathbf{b}_f \cdot \mathbf{b}_f$. The tensor contraction in (40) is evaluated in matrix arithmetic:

$$\begin{aligned} e_f^1 : \mathbf{A}_{\tilde{\omega}} : e_f^2 &= \lambda_0 \text{tr} e_f^1 \text{tr} e_f^2 + 2\mu \text{tr}(e_f^1 e_f^2) \\ e_f^1 : \mathbf{B}_{\tilde{\omega}} : e_f^2 &= \lambda_0 \left(\text{tr}(\mathbf{b}_f e_f^1) \text{tr} e_f^2 + \text{tr}(\mathbf{b}_f e_f^2) \text{tr} e_f^1 \right) + 4\mu \text{tr}(\mathbf{b}_f e_f^1 e_f^2), \end{aligned}$$

where e_f^1, e_f^2 denote arbitrary symmetric matrices on face f .

Similarly, the discretization of \dot{I}_{ijkl}^s in (27) is given by

$$\begin{aligned} \dot{I}_{ijkl}^s &\approx \sum_{f \in \mathcal{F}} \sum_{q \in N(f)} v_n^q \int_f 2\phi_q \left[B^h(\mathbf{u}_{ij}^h, \mathbf{u}_{kl}^h) - \frac{\text{tr} \mathbf{b}_f}{2} A^h(\mathbf{u}_{ij}^h, \mathbf{u}_{kl}^h) \right] \\ &\quad + C_q^h(\mathbf{u}_{ij}^h, \mathbf{u}_{kl}^h) + C_q^h(\mathbf{u}_{kl}^h, \mathbf{u}_{ij}^h). \end{aligned}$$

E Isotropic penalty

For cubic symmetric shell lattice, the isotropic condition is typically satisfied by minimizing or constraining the error between Zener ratio [Zener 1948] and 1. Since the input surface is generally not cubic symmetric, we adopt a different approach. Note that the isotropic elastic tensors have the following form

$$\mathbb{C} = \lambda \delta^{ij} \delta^{kl} + \mu \left(\delta^{ik} \delta^{jl} + \delta^{il} \delta^{jk} \right).$$

Therefore, they constitute a two-dimensional linear space spanned by two tensors

$$\mathbb{C}_\lambda := \delta^{ij} \delta^{kl}, \quad \mathbb{C}_\mu := \delta^{ik} \delta^{jl} + \delta^{il} \delta^{jk}.$$

We penalize the anisotropy of ADS by adding the following penalty term to the objective

$$f_{iso}^s(\mathbb{C}_A) = \min_{\lambda, \mu} \frac{1}{2} \|\mathbb{C}_A - (\lambda \mathbb{C}_\lambda + \mu \mathbb{C}_\mu)\|_F^2. \quad (41)$$

The time derivative of this function is given by

$$\frac{d}{dt} f_{iso}^s(\mathbb{C}_A) = [(\lambda^* \mathbb{C}_\lambda + \mu^* \mathbb{C}_\mu) - \mathbb{C}_A] :: \dot{\mathbb{C}}_A,$$

where λ^*, μ^* denote the minimizer of (41) and ‘::’ denotes tensor contraction.

F Objective for negative Poisson’s ratio

We minimize the following objective function to design shell lattices with negative Poisson’s ratios

$$f(\mathbb{C}_A) = \epsilon_1(\mathbb{C}_A) + \epsilon_2(\mathbb{C}_A).$$

Here, ϵ_1, ϵ_2 denote the lateral contractions in two orthogonal directions when the material is stretched. We approximate them by solving the following problem based on the the principle of minimal potential energy:

$$\min_{\epsilon_1, \epsilon_2} F(\epsilon_1, \epsilon_2) : \mathbb{C}_A : F(\epsilon_1, \epsilon_2), \quad (42)$$

where

$$F(\epsilon_1, \epsilon_2) = \begin{pmatrix} -\epsilon_1 & 0 & 0 \\ 0 & -\epsilon_2 & 0 \\ 0 & 0 & 1 \end{pmatrix}.$$

Equation (42) is a least square problem, whose solution can be readily found by solving a linear system.